

國立臺灣大學理學院大氣科學研究所

碩士論文

Department of Atmospheric Sciences

College of Science

National Taiwan University

Master Thesis



南亞高壓的準地轉位渦觀點

Quasi-Geostrophic Potential Vorticity Perspective

on South Asian High

黃品鈞

Pin-Chun Huang

指導教授：郭鴻基 博士

Advisor : Hung-Chi Kuo, Ph.D.

中華民國 110 年 08 月

August, 2021

誌 謝



這篇論文的完成，代表自己碩士班生涯總算告一段落。回首自己這三年間，不僅僅是學術上的工作，還有許多家中的煩心事需要處理；而最後能夠堅持下去，完成一份完整的、對科學進展有幫助的研究，需要感謝的人們太多了。

感謝郭鴻基老師對論文的指導，在這段期間我們不斷嘗試各式各樣的題目、診斷方式，而最終能有一個令自己自豪的結果；我想郭老師帶給我的是那對研究一絲不苟的態度，以及和老師討論時徹底感受到的對知識的喜悅，使我能在學術這條路上繼前行。感謝口試委員：楊明仁老師、簡芳菁老師、陳世楠老師，以及來幫忙的梁禹喬老師給予論文的寶貴建議，讓本論文更為完整。

感謝徐驊學姊各種研究與程式上的幫忙；謝謝鴻睿學長、郁涵學姊時常感與研究上的建議；謝謝達剴這個從物理系就結交的好朋友兼實驗室同學，能夠一起討論研究、討論哲學、討論 JOJO；謝謝婉瑜、顥瑄、亭祐，有你們在替研究室添加了許多歡樂。謝謝亦詩、庭維、禎晏這群從大學時就一起修課的朋友們，尤其感謝 YP 在論文的數學上給予許多指點。感謝舒凡、冠宇、俊儒等物理系好朋友，也祝各位在研究或業界能一帆風順。謝謝廷涓提供心理上的支持，也謝謝地球科學奧林匹亞的所有人，除了是我地科之路的起點，而每當自己陷入困境中，總能在過去的記憶中找回自己的初衷。

感謝美雲總是超辛苦的處理實驗室大小事，堪稱實驗室保母；感謝超有耐心的國豐助教，這段期間麻煩各種行政事務了。最後，感謝我的家人，能夠無條件地支持我追尋自己的夢。

黃品鈞 謹誌於
動力模擬研究室

2021/8/20

摘要



南亞高壓為夏季活躍於中緯度歐亞大陸對流層頂之高壓系統。青藏高原之非絕熱加熱與其形成和維持息息相關，多年來有大量研究探討青藏高原的加熱與南亞高壓強度以及其東西震盪之關聯性。然而，前人之大量研究針對南亞高壓之位勢高度進行統計分析，而甚少探討南亞高壓的位渦性質。

本研究試圖建立南亞高壓的位渦觀點。位渦同時包含了動量與質量場資訊，對於中大尺度天氣系統是很好的診斷工具。參考 Schubert *et al.* (2009) 所提出的準地轉全球淺水位渦模式，我們建立了利用類球諧函數作為基底的理想模式。該模式成功解決了在赤道無科氏力而無法使用準地轉近似的問題。我們首先簡介位渦的性質，包含了其守恆性與反演定律，並比較傳統上 f -plane 與 β -plane 近似下之位渦與此全球模式之位渦的異同。

我們利用 ECMWF 的再分析資料(ERA5)計算青藏高原與東亞季風區的非絕熱加熱，以及由此所生成之負位渦異常。我們參考了 Hsu and Plumb (2000) 的做法，利用理想模式，探討了在有背景流的狀況下，在青藏高原施加固定的熱源，考慮非線性作用時的渦旋洩離過程。該過程是造成南亞高壓東西不對稱性與兩個中心的原因；一個中心位在青藏高原上方，另一個則在伊朗高原上方。在 150 hPa 位勢高度圖上，僅能觀察到中心的東西震盪，而利用 370 K 之等熵位渦圖分析，則可以看到明顯的渦旋洩離過程。

特別地，研究者們亦關注南亞高壓之強度與中心位置如何影響東亞地區之降雨。然而，對於東亞地區之降雨如何反過來影響南亞高壓之強度，卻甚少有研究進行探討。我們針對 1979-2020 夏季之月平均 370 K 等熵面位渦圖做正交經驗函數分析，以尋找南亞高壓位渦的年變異情形。結果顯示，其第一個模之變異度最大值並不在南亞高壓的本體位置，而是自東亞季風區延伸至南亞的帶狀圖形。我們推測東亞地區的降雨是造成南亞高壓位渦年變化的主因之一。東亞地區的降雨與南亞高壓位渦之變異度

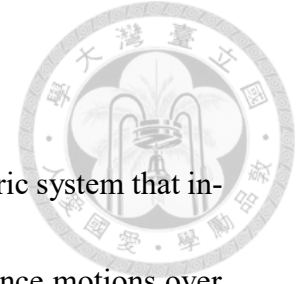
在統計上亦有相關性。此為前人研究所未觀察到之現象，我們推測是因為位渦場的資訊在低緯度地區無法反映在質量場的變化上。

在理想模式的實驗設計上，我們將原先渦旋逸離實驗之青藏高原熱源東側加上強度強但空間尺度較小之熱源。結果顯示東亞季風區形成之位渦會被併入青藏高原的主位渦之中，並造成整體位渦之增強，增加之形狀與正交經驗函數分析之第一個模相似。由於能反映出低緯度地區質量場看不到的資訊，我們認為此全球淺水位渦模式極其適用於亞熱帶地區的氣候診斷。同時，亦發現到東亞地區增加的負渦度異常會拖慢整體渦旋逸離之速度。儘管我們無法從南亞高壓月平均的東西偏移和降雨量找出相關係數，但值得注意的是，強降雨年的南亞高壓月平均高壓中心都不位於西邊。

我們還發現到南亞高壓的中心位置與高層空氣沉降有密切的關係，無論中心偏西、偏東或是雙中心，都可以看到高壓東側會有上升運動而西側有明顯的沉降運動。此現象可能可以更進一步改良「乾者越乾，濕者越濕」之季風-沙漠耦合現象，值得更進一步的探討。

關鍵字: 南亞高壓、淺水方程、準地轉理論、位渦、東亞季風、渦旋逸離


Abstract



South Asian high (SAH) is a planetary-scale upper-tropospheric system that influences the Asian summer monsoon (ASM) rainfall and subsidence motions over the Sahara Desert and Mediterranean in boreal summer. As an essential topic in dynamical climatology, it still lacks understanding under the perspective of quasi-balanced dynamics. In this thesis, we give a thorough review on the concept of quasi-geostrophic (QG) theory and potential vorticity (PV). We introduce the global shallow water quasi-geostrophic (SWQG) model as the tool for planetary-scale potential vorticity (PV) evolution simulation. The properties and advantages of this idealized model are studied comprehensively in this article.

We review the characteristics of SAH, with the calculation of heating and dynamical structures of the upper troposphere above the Tibetan plateau (TP) and ASM area from ECMWF Reanalysis v5 (ERA5) data. The zonal asymmetric structure of SAH caused by vortex-shedding process, which is not well discussed in early research, is under investigation as well. We conclude that the non-linearity of PV serves as an essential factor of the weekly-scale vortex-shedding process, while the zonal oscillation and asymmetry structure is corresponded on geopotential map.

Indices of the intensity and location of SAH are built. We analyze the variabilities of SAH and find that severe precipitation over the Yangtze River (YR) valley



has a linkage with the intensification of SAH. We attribute this phenomenon to the enhancement of PV forcing over YR region. Model simulations have verified that PV forcing over YR region would be absorbed by the main structure over TP, and the Empirical Orthogonal Function (EOF) analysis results show the correlation between YR rainfall and the intensity of SAH PV. We claim that the PV forcing caused by YR precipitation can only be observed on PV map, due to the lack of mass response signal in the lower latitude when geopotential height analysis. An interesting simulation result is that the PV forcing over YR region may postpone the vortex-shedding process. This may be the reason why SAH center prefers staying eastward during YR strong precipitation years.

Additionally, we analyze the relationship between the location of SAH and the vertical motions, and the results can be well-explained based on Sverdrup balance theory. The traditional monsoon-desert coupling may be revised with this discovery. At the end, we discuss how PV perspective promote our understanding on SAH.

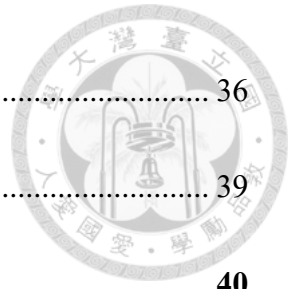
Keywords: South Asian high, shallow water system, quasi-geostrophic theory, potential vorticity, Asian summer monsoon, vortex-shedding

Contents



口試委員審定書	II
誌 謝	II
摘 要	III
Abstract.....	V
Contents.....	VII
List of Figures.....	IIIX
List of Tables	XII
1. Introduction	1
2. Introduction to QGPV Dynamics	5
2.1 Shallow Water Quasi-Geostrophic Theory	6
2.2 Global Quasi-Geostrophic Theory.....	10
2.2.2 Validity of the Global SWQG Theory	12
2.2.3 Physical Explanation	15
2.2.4 Solution with Spheroidal Harmonics.....	17
3. The SW-QGPV Model on the Sphere	20
3.1 Model Construction	20
3.3 Model Performance	24
3.3.2 Linear Rossby Wave Propagation.....	26

3.4 Model with Topography	36
3.5 Usage of the global SWGQ model	39
4. The PV perspective of South Asian High.....	40
4.1 Introduction and Methodology	40
4.2 The Heating Structure of SAH	41
4.3 The PV forcing of SAH	44
4.4 The Vortex-Shedding Process and SAH	48
4.5 SAH and the Precipitation of Yangzi River Valley.....	54
4.6 SAH and the Vertical Motion above Eurasian.....	60
5. Conclusion	62
Reference.....	65
Appendix A. Spherical and Spheroidal Harmonics.....	68
Appendix B. Programming of the Global SWQG model.....	72



List of Figures

- Figure 1.** The extra term component $2\Omega a \sin\phi - 1g \cot\phi$ changing with latitude. We can see that at the vicinity of the equator, the component grows dramatically. 14
- Figure 2.** (a) Spherical harmonics and (b) Spheroidal harmonics ($\varepsilon = 100$) with different wave numbers. The spheroidal harmonics looks just like the spherical harmonics being compressed on the zonal direction..... 19
- Figure 3.** The flow chart for solving the spheroidal harmonic based global SWQG model. 22
- Figure 4.** The grid points on (a) (λ, ϕ) coordinate and (b) (λ, μ) coordinate. We should notice that on the area at high latitude is compressed, while area at the low latitude is stretched on the (λ, μ) coordinate. 23
- Figure 5.** The elliptical PV anomaly located at 45 °N (dotted thick contour, in s^{-1}) and its streamfunction (shading, in m^2s^{-1}) of (a) non-divergent barotropic model and (b) SWQG_E300. We can see that with a stronger mass response (the stronger screened effect), the streamfunction becomes smaller, localized, and its contour becomes more parallel to the contour of the PV anomaly. 30
- Figure 6.** (a) The circular PV anomaly located at 45 °N (shading, in s^{-1}), its streamfunction (blue dotted contour, in m^2s^{-1}), and its height anomaly (black contour, in m) under SWQG_E300. (b) Left: the zonal component of the non-divergent wind, geostrophic wind, and their difference from top to bottom. Right: same as the left but for the meridional component..... 31
- Figure 7.** (a) The PV anomaly caused by heating located at the equator (shading, in s^{-1}), its streamfunction (blue dotted contour, in m^2s^{-1}), and its height anomaly (black contour, in m) under SWQG_E300. (b) Left: the zonal component of the non-divergent wind, geostrophic wind, and their difference from top to bottom. Right: same as the left but for the meridional component..... 32
- Figure 8.** Isolines of the “quasi-geostrophic frequency correction factor” for $\varepsilon=10, 100, 1000$ and 10000. Adapted from Schubert *et al.* (2009). 33
- Figure 9.** (a) The initial circular PV anomaly located at 30 °N (shading, in s^{-1}). (b) Upper: PV anomaly after 10 days of integration under SWQG_E9. Down: PV anomaly after 10 days of integration under SWQG_E300. (c) Same as (b), but for height anomaly..... 34
- Figure 10.** Upper: the PV anomaly (shading, in s^{-1}) of the super-rotational flow experiment with topography (circled with magenta), conducted with SWQG_E9. Below: the original result from Grose and Hoskins (1979), where contour is the vorticity anomaly. Note that PV anomaly and vorticity anomaly are almost the same in the external mode, due to lack of mass reponse. 37

Figure 11. Same as fig. 10, but with height anomaly (shading, in m). Mass adaption are significant at higher latitudes.....	38
Figure 12. The July mean (a) geopotential height (shading, in gpm) and (b) PV (shading, in PVU) of the SAH, averaged from 1979 to 2020.	43
Figure 13. The July monthly mean vertical distribution of the apparent heating rate Q_1/c_p (red) and the moist heating rate Q_2/c_p (blue) for (a) Tibetan Plateau, averaged from 1979 to 2020, (b) Yangzi River valley, averaged from 1979 to 2020, and (c) Yangzi River valley at 2020, with red dotted line to be 42- year averaged Q_1/c_p for comparison. Heating structure of TP below 600 hPa are below the ground and may not be realistic.....	43
Figure 14. July mean zonal vertical profile at 30°N with isentropes (contour, in K), PV (shading, in PVU), and vertical velocity (arrow, in Pa/s) averaged from 1979 to 2020. (b) The schematic diagram of how the PV anomaly forms under PV perspective with isentropes (blue line), PV contour (red line), and horizontal wind direction (black symbols). (c) The schematic diagram of how apparent heating creates PV forcing.	45
Figure 15. (a) July mean PV forcing (shading, in PVU/day) and PV (contour) at 370 K averaged from 1981 to 2020. (b) July monthly mean land precipitation (shading, in mm/day) averaged from 1981 to 2020.	47
Figure 16. Top: July mean geopotential (shading, in m^2s^2) on 150 hPa surface at 1979 (left), a western-type SAH and 1982 (right), an eastern-type SAH. Down: July mean PV (shading, in PVU) on 370K surface with geopotential on 150 hPa (contour, in m^2s^2) at 1979(left), a western-type SAH and 1982 (right), an eastern-type SAH.	51
Figure 17. (a) The experiment design for SAH daily simulation with location of forcing (shading) and background vorticity (contour), which does not evolve with time. (b) SWQG model result time series with PV anomaly (shading, in s^{-1}) and height anomaly (contour). (c): reanalysis data with PV on 370 K (shading, in PVU), and geopotential on 150hPa (contour).....	52
Figure 18. Hovmuller diagram of geopotential height (shading, in gpm) at 150 hPa surface along 30°N at 2020 summer.....	53
Figure 19. (a) SWQG model result with PV anomaly (shading, in s^{-1}) and background PV (contour) consider pure advection, integrated for 5 days. (b) Schematic diagram of the vortex-shedding dynamics.....	53
Figure 20. (a) The pattern of first mode of SAH PV in July under EOF analysis (shading). (b) Correlation between Julys mean precipitation over YR (blue) and amplitude of the first mode (orange).	57
Figure 21. (a) Same as fig. 17 (a), but adding an extra forcing above YR valley. (b)	

SWQG model result with PV anomaly (shading, in s^{-1}) and height anomaly (contour) adding YR forcing, integrated for 5 days. (c) same as (b), but without YR forcing.....	58
Figure 22. The 5-7 days averaged PV difference (shading, in s^{-1}) between the pure TP forcing experiment and YR forcing added experiment. The YR forcing would enhance the PV intensity of SAH.	58
Figure 23. The sensitivity test of the YR valley forcing with the translation speed. The amplitude of YR forcing is set to be $-6 \times 10^{-5} s^{-1} / day \times \text{Forcing Factor}$.59	
Figure 24. ω (shading, in Pa/s) and geopotential height (contour) patterns at (a) western type (b) eastern type (c) double centered of SAH.	61

List of Tables

Table 1. Different vertical modes, the equivalent depths, gravity wave speeds associated with different Lamb's parameter.	16
Table 2. Different kinds of potential vorticity anomaly. We can see SW-QGPV on the sphere having analogy to SW-QGPV on β -plane, except for the Coriolis force applied on the whole globe.	17
Table 3. PV conservation principles on the Cartesian coordinate and on the globe. The two equations are both consists of non-linear advection term and linear Rossby wave term.	17

CHAPTER 1

Introduction



South Asian high (SAH) is an upper-tropospheric anticyclonic system elongating from the East Asia to the Sahara Desert in boreal summer. It is well recognized that the Tibetan plateau (TP) exerts intense and persistent diabatic heating (with both sensible heat flux and latent heat release) to the atmosphere which gives rise to the formation and maintenance of SAH. (He *et al.*, 1987; Yanai and Lee, 1994; Liu *et al.*, 2001; Duan *et al.*, 2005). Originating from the East of Eurasia, this thermally driven circulation may affect the subsidence over the Mediterranean and the Sahara Desert, which is well known as the monsoon-desert coupling mechanism proposed by Rodwell and Hoskins (1996; 2001) under the linear dynamic regime.

However, the relationship between SAH and precipitation over East Asia is not fully understood. Ning *et al.* (2017) specified the positive correlation between SAH intensity and precipitation over the Yangtze River (YR) valley; Ge *et al.* (2019) discovered that YR precipitation has strong connection to TP forcing and SAH intensity, while a weak connection to SAH location. However, those statistical results could not answer that it is either the intensification of SAH enhances the precipitation, or the increase of

precipitation strengthens SAH, or even both. Ning *et al.* (2017) proposed that the intensifying of SAH would deepen the trough over YR valley due to stronger Rossby wave dispersion and increase the rainfall, while Ge *et al.* (2019) hypothesized that strong TP thermal forcing would strengthen the jets and convergence near YR valley on the ground. Both of the articles are lack of model simulation as a verification.

As mentioned by Hoskins (2015), potential vorticity (PV) may be a useful tool for us to understand SAH. Different from former research that usually diagnose SAH through its geopotential height anomaly, this thesis aims to build a PV perspective on SAH. PV, introduced by Rossby (1939) and Ertel (1942) in its full-hydrodynamic form, has its splendid properties listed below:

- (1) *Conservative*. Total PV bounded by two isentropic surface obeys the conservation law. That is to say, PV cannot be created or destroyed within two layers, but can only be diluted or concentrated by cross-isentropic mass inflow or outflow (Haynes and McIntyre, 1987).
- (2) *Invertible*. Given the information of PV distribution in a specified domain, we can recover the mass and momentum fields by the invertibility principle in an approximate balanced condition.

The quasi-geostrophic potential vorticity (QGPV), derived by Charney and Stern (1962), may be one of the most elegant reduction in dynamical meteorology. As “a

major weapon in the armory of atmospheric scientists” (Hoskins, 2015), the traditional QGPV approximation still has its limits: singularity on the equator and errors from the linear approximation of the Coriolis force. To solve these problems, Schubert *et al.* (2009) and Verkley (2009) constructed the globalized SWQG theory, and the solutions are spheroidal harmonics in the spectrum space. This model then could serve as an appropriate tool for dragonizing this enormous system.

We will start from a comprehensive review over the history and formulation of PV and QG theory in Chapter 2. A detailed derivation of globalized SWQG theory is included, and we would test the validity of this brand-new model through some classical idealized experiments in Chapter 3. The results are compared with the non-divergent barotropic model, and the physical meanings behind would be discussed.

We will give an overview on SAH in Chapter 4, including its PV and geopotential characteristics on both monthly and daily scales. The vertical heating structure and PV forcing on 370K isentropic surface over TP and YR region is calculated. The asymmetry and vortex-shedding problem of SAH (Hsu and Plumb, 2000) will be revisited using this brand-new model. We will show how vortex-shedding process produces double PV center of SAH in a weekly scale, producing asymmetry of monthly mean SAH pattern, and how this process is observed as the zonal oscillation on the geopotential height map.

To see how annual variations of SAH connect with YR precipitation variability, the

monthly mean SAH intensity and location are organized into indices and correlated with YR valley summer rainfall. Traditional method defines the area of SAH on the geopotential height map as the strength of SAH. In this research, we introduce the empirical orthogonal function (EOF) analysis on isentropic potential vorticity (IPV) map as a new insight describing the SAH intensity. A new signal at the lower latitude that has never been discussed appears if using the PV diagnosing method. After that, we will try to explain what causes the linkage between SAH intensity and YR valley rainfall, with physical explanation and idealized model simulation result. Additionally, we would discuss the relationships between vertical motions over mid-latitude Eurasia and the shape of SAH. We will give some suggestion on the revision of monsoon-desert coupling mechanism. The conclusions are listed in Chapter 5.

CHAPTER 2

Introduction to QGPV Dynamics



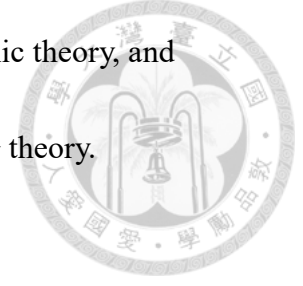
“I personally regard the successful reduction of the dynamic equations to a single prognostic equation by means of the geostrophic relationship as the greatest single achievement of twentieth century dynamic meteorology.”

—— Edward Lorenz (2006)

The concept of potential vorticity (PV), first conceived in a single layer of shallow water by Rossby in 1939, and in an idealized continuous fluid by Ertel in 1942, is undoubtedly one of the most celebrated milestones in theoretical meteorology. With the combination of quasi-geostrophic (QG) approximation, formulated by Charney and Stern in 1962, QGPV is one of the simplest but most insightful reduction to the large-scale dynamical systems of the Earth. Under the framework of quasi-balance dynamics, the large-scale motions are governed entirely by the self-evolution of PV, which is a materially conserved quantity.

Although its elegance had made PV a useful tool on weather and climate analysis, the generalization of QGPV on the entire sphere had long been silent until Schubert *et al.* (2009) and Verkley (2009) stood up for its application individually. In this chapter,

I will give a brief introduction to the shallow water quasi-geostrophic theory, and would go through Schubert and Verkley's latest work on global QG theory.



2.1 Shallow Water Quasi-Geostrophic Theory

The dimensional form of shallow water equations on the Cartesian coordinate

(x^*, y^*) can be written as follows

$$\frac{\partial u^*}{\partial t^*} + u^* \frac{\partial u^*}{\partial x^*} + v^* \frac{\partial u^*}{\partial y^*} - f v^* = -g \frac{\partial h^*}{\partial x^*}, \quad (2.1.1)$$

$$\frac{\partial v^*}{\partial t^*} + u^* \frac{\partial v^*}{\partial x^*} + v^* \frac{\partial v^*}{\partial y^*} + f u^* = -g \frac{\partial h^*}{\partial y^*}, \quad (2.1.2)$$

$$\frac{\partial h^*}{\partial t^*} + u^* \frac{\partial (h^* - \eta^*)}{\partial x^*} + v^* \frac{\partial (h^* - \eta^*)}{\partial y^*} + (H + h^* - \eta^*) \left(\frac{\partial u^*}{\partial x^*} + \frac{\partial v^*}{\partial y^*} \right) = -g \frac{\partial h^*}{\partial y^*}, \quad (2.1.3)$$

where u^* is the eastward component of velocity, v^* the northward component, h^* the deviation of the fluid depth from the mean depth H , η^* the topography, g the acceleration of gravity, and f the Coriolis parameter. Set $f = f_0$ to be a constant, the non-dimensional forms of the equations are

$$\frac{U}{T} \frac{\partial u}{\partial t} + \frac{U^2}{L} \left(u \frac{\partial}{\partial x} + v \frac{\partial}{\partial y} \right) u - f_0 U v = -g \frac{N_0}{L} \frac{\partial h}{\partial x}, \quad (2.2.1)$$

$$\frac{U}{T} \frac{\partial v}{\partial t} + \frac{U^2}{L} \left(u \frac{\partial}{\partial x} + v \frac{\partial}{\partial y} \right) v - f_0 U u = -g \frac{N_0}{L} \frac{\partial h}{\partial y}, \quad (2.2.2)$$

$$\frac{N_0}{T} \frac{\partial h}{\partial t} + \frac{U}{L} \left(u \frac{\partial}{\partial x} + v \frac{\partial}{\partial y} \right) (N_0 h - H \eta) + \frac{U}{L} (H + N_0 h - H \eta) \left(\frac{\partial u}{\partial x} + \frac{\partial v}{\partial y} \right) = 0, \quad (2.2.3)$$

with $(u, v) = \frac{(u^*, v^*)}{U}$, $t = \frac{t^*}{T}$, $L(x, y) = L(x^*, y^*)$, $h = \frac{h^*}{N_0}$, $\eta = \frac{\eta^*}{H}$; U, T, L, N_0 are

characteristic velocity, time, length and height anomaly scale, respectively. Under the

geostrophic balance condition $gh^* = f_0 \psi$, with ψ denoting the stream function of

the non-divergent part of the flow ($u_\psi = -\frac{\partial\psi}{\partial y}$, $v_\psi = \frac{\partial\psi}{\partial x}$), we get $N_0 = \frac{f_0 UL}{g}$. Fol-

lowing the arguments of Charney and Stern (1962), we are interested in modes that

are quasi-geostrophic, which means that the Rossby number $Ro = \frac{U}{f_0 L} \ll 1$, and the

characteristic time scale has the same order with the advective time scale ($T \sim \frac{L}{U}$). We

may define $\epsilon = Ro = \frac{U}{f_0 L}$ and $\epsilon_T = \frac{1}{f_0 T}$ with $\epsilon \sim \epsilon_T \ll 1$. The equations can be

simplified to

$$\epsilon_T \frac{\partial u}{\partial t} + \epsilon \left(u \frac{\partial}{\partial x} + v \frac{\partial}{\partial y} \right) u - v = -\frac{\partial h}{\partial x}, \quad (2.3.1)$$

$$\epsilon_T \frac{\partial v}{\partial t} + \epsilon \left(u \frac{\partial}{\partial x} + v \frac{\partial}{\partial y} \right) v + u = -\frac{\partial h}{\partial y}, \quad (2.3.2)$$

$$\epsilon_T F \frac{\partial h}{\partial t} + (\epsilon F h - \eta) \left(u \frac{\partial}{\partial x} + v \frac{\partial}{\partial y} \right) + (1 + \epsilon F h - \eta) \left(\frac{\partial u}{\partial x} + \frac{\partial v}{\partial y} \right) = 0, \quad (2.3.3)$$

where $F = \frac{f_0^2 L^2}{gH} = \frac{L^2}{\lambda_R^2}$. Expand the variables in an asymptotic series with the Rossby

number as the small parameter

$$u = u_0 + u_1 \epsilon + O(\epsilon^2), \quad (2.4.1)$$

$$v = v_0 + v_1 \epsilon + O(\epsilon^2), \quad (2.4.2)$$

$$h = h_0 + h_1 \epsilon + O(\epsilon^2), \quad (2.4.3)$$

$$\eta = \eta_0 + \eta_1 \epsilon + O(\epsilon^2), \quad (2.4.4)$$

and plug them into (2.3.1) ~ (2.3.3), we can get the results below. For $O(1)$, we get

$$v_0 = \frac{\partial h_0}{\partial x} \quad (2.5.1)$$

$$u_0 = -\frac{\partial h_0}{\partial y} \quad (2.5.2)$$

$$u_0 \frac{\partial \eta_0}{\partial x} + v_0 \frac{\partial \eta_0}{\partial y} = 0 \quad (2.5.3)$$

to be the “geostrophic balance”, meaning that the Coriolis force is totally balanced to the pressure gradient force, and the winds are parallel to the isobars. Combining

(2.5.1) and (2.5.2) gives $\nabla \cdot \mathbf{u}_0 = 0$, so the velocity field is divergence-free. For $O(\epsilon)$,

we get

$$\frac{\partial u_0}{\partial t} + \left(u_0 \frac{\partial}{\partial x} + v_0 \frac{\partial}{\partial y} \right) u_0 - v_1 = -\frac{\partial h_1}{\partial x} \quad (2.6.1)$$

$$\frac{\partial v_0}{\partial t} + \left(u_0 \frac{\partial}{\partial x} + v_0 \frac{\partial}{\partial y} \right) v_0 + u_1 = -\frac{\partial h_1}{\partial y} \quad (2.6.2)$$

$$F \left(\frac{\partial}{\partial t} + u_0 \frac{\partial}{\partial x} + v_0 \frac{\partial}{\partial y} \right) h_0 - \left(u \frac{\partial}{\partial x} + v \frac{\partial}{\partial y} \right) \eta + \left(\frac{\partial u_1}{\partial x} + \frac{\partial v_1}{\partial y} \right) = 0. \quad (2.6.3)$$

These are the non-dimensional quasi-geostrophic shallow water equations. By cross

differentiating (2.6.1) and (2.6.2), we would get

$$\left(\frac{\partial}{\partial t} + u_0 \frac{\partial}{\partial x} + v_0 \frac{\partial}{\partial y} \right) \zeta_0 + \left(\frac{\partial u_1}{\partial x} + \frac{\partial v_1}{\partial y} \right) = 0, \quad (2.7)$$

where $\zeta_0 = \frac{\partial v_0}{\partial x} - \frac{\partial u_0}{\partial y}$. Also, by cross differentiating (2.5.1) and (2.5.2), we obtain

$$\zeta_0 = \nabla^2 h_0. \quad (2.8)$$

Define $D = \left(\frac{\partial u_1}{\partial x} + \frac{\partial v_1}{\partial y} \right)$ and $D_g = \left(\frac{\partial}{\partial t} + u_0 \frac{\partial}{\partial x} + v_0 \frac{\partial}{\partial y} \right)$, (2.6.3) and (2.7) can be

combined and written as

$$D_g(\nabla^2 h_0 - F h_0 + \eta) = 0. \quad (2.9)$$

The value $(\nabla^2 h_0 - F h_0 + \eta)$ is then to be conservative. This is the non-dimensional

shallow water quasi-geostrophic potential vorticity (SW-QGPV) conservation equa-

tion on the f -plane. Restoring the dimensions, (2.9) becomes

$$\frac{D}{Dt} \left(\nabla^2 \psi - \frac{1}{L_R^2} \psi + f \frac{\eta^*}{H} \right) = 0 \quad (2.10)$$

where $\psi = \frac{g}{f_0} h$, $L_R = \frac{\sqrt{gH}}{f_0}$ to be the Rossby radius of deformation, and $\frac{D}{Dt} = \frac{\partial}{\partial t} + u_g \frac{\partial}{\partial x} + v_g \frac{\partial}{\partial y}$. If we set $f = f_0 + \beta y$ in (2.1.1) and (2.1.2), we would obtain the

QGPV conservation rule on the β -plane

$$\frac{D}{Dt} \left(\nabla^2 \psi - \frac{1}{L_R^2} \psi + \beta y + f \frac{\eta^*}{H} \right) = 0. \quad (2.11)$$

The pedagogical and calculational advantages of quasi-geostrophic theory is well recognized with concise equations providing invaluable insight on synoptic scale weather systems. However, in the traditional textbook approach, the theory does not apply on the globe. That is, the Coriolis force would vanish on the equator and causes singularity for the quasi-geostrophic assumption. Matsuno (1966), in his famous article “Quasi-Geostrophic Motions in the Equatorial Area”, had pointed out that motions on the equator does follow the quasi-geostrophy:

“Those peculiarities found in the Rossby type solution might simply be attributed to vanishing of the Coriolis force. Anyhow it is noteworthy that we can get " quasi-geostrophic "motions in the domain including the equator.”

So, what is the trick for obtaining the global balanced theory?

2.2 Global Quasi-Geostrophic Theory

2.2.1 Formulation



Schubert *et al.* (2009) and Verkley (2009) had figured out the solution of the generalization of SWQG theory on the sphere theoretically without topography, and we will first present the derivation from their articles, but with more mathematical details.

The shallow water primitive equations on the spherical coordinate (λ, ϕ) could be written as

$$\frac{Du}{Dt} - \left(2\Omega \sin\phi + u \frac{\tan\phi}{a} \right) v + g \frac{1}{a \cos\phi} \frac{\partial h}{\partial \lambda} = 0, \quad (2.12.1)$$

$$\frac{Dv}{Dt} + \left(2\Omega \sin\phi + u \frac{\tan\phi}{a} \right) u + g \frac{1}{a} \frac{\partial h}{\partial \phi} = 0, \quad (2.12.2)$$

$$\frac{Dh}{Dt} + \frac{(H+h)}{a \cos\phi} \left(\frac{\partial u}{\partial \lambda} + \frac{\partial(v \cos\phi)}{\partial \phi} \right) = 0, \quad (2.12.3)$$

where u is the eastward component of velocity, v the northward component, h the deviation of the fluid depth from the global mean depth H , Ω the earth's rotation rate, a the earth's radius, g the acceleration of gravity, and $\frac{D}{Dt} = \frac{\partial}{\partial t} + u \frac{\partial}{a \cos\phi \partial \lambda} + v \frac{\partial}{a \partial \phi}$ the material derivative. By cross differentiating (2.12.1) and (2.12.2) then substitute into (2.12.3) yields the PV conservative equation

$$\frac{DP}{Dt} = 0, \quad (2.13)$$

where P is the potential vorticity on the sphere given by

$$P = \left(\frac{H}{H+h} \right) \left(2\Omega \sin\phi + \left(\frac{\partial v}{a \cos\phi \partial \lambda} - \frac{\partial(u \cos\phi)}{a \cos\phi \partial \phi} \right) \right). \quad (2.14)$$

Now here is the trick. Rather than partitioning the flow into geostrophic and ageostrophic part that requires the small Rossby number approximation, the key point is to assume that the non-divergent part of the flow is much larger than the irrotational part, i.e., $u_\psi \gg u_\chi$. We would discuss the validity of this trick later. The non-divergent flow can be written as

$$\begin{aligned} (u_\psi, v_\psi) &= \left(-\frac{\partial\psi}{a\partial\phi}, \frac{\partial\psi}{a\cos\phi\partial\lambda} \right) \\ &= \left(-\sqrt{1-\mu^2} \frac{\partial\psi}{a\partial\mu}, \frac{1}{\sqrt{1-\mu^2}} \frac{\partial\psi}{a\partial\lambda} \right). \end{aligned} \quad (2.15)$$

with $\mu = \sin\phi$ and ψ denoting the stream function for the non-divergent part of the flow. Plug (2.15) into (2.14) can get PV represented by height and stream function

$$P = 2\Omega\mu + \left(\frac{H}{H+h} \right) \nabla^2\psi - 2\Omega\mu \left(\frac{h}{H+h} \right), \quad (2.16)$$

where $\nabla^2 = \frac{1}{a^2} (1-\mu^2) \frac{\partial^2}{\partial\mu^2} + \frac{1}{a^2} \frac{1}{1-\mu^2} \frac{\partial^2}{\partial\lambda^2}$. We may assume the height anomaly is

small enough, i.e. $|h| \ll H$ and $\nabla^2\psi \ll 2\Omega\mu$, then (2.16) reduces to

$$\begin{aligned} P &\approx 2\Omega\mu + \nabla^2\psi - \nabla^2\psi \left(\frac{h}{H} \right) - 2\Omega\mu \left(\frac{h}{H} \right) \\ &\approx 2\Omega\mu + \nabla^2\psi - 2\Omega\mu \left(\frac{h}{H} \right) \\ &= 2\Omega\mu + q \end{aligned} \quad (2.17)$$

where q is the potential vorticity anomaly $\nabla^2\psi - 2\Omega\mu \left(\frac{h}{H} \right)$. We may assume that ψ

and h are related by the linear balance condition (Charney and Stern, 1962)

$$\nabla \cdot (2\Omega\mu \nabla\psi) = g\nabla^2 h \quad (2.18)$$

and consider the Coriolis force $2\Omega\mu$ is small varying with space (comparing to $\nabla\psi$

and ∇h), we can apply the local linear balance condition

$$gh = 2\Omega\mu\psi. \quad (2.19)$$

Substitution of (2.17) and (2.19) into (2.13) yields

$$\frac{\partial q}{\partial t} + \frac{1}{a^2} \frac{\partial(\psi, q)}{\partial(\lambda, \mu)} + \frac{2\Omega}{a^2} \frac{\partial\psi}{\partial\lambda} = 0 \quad (2.20)$$

$$q = \nabla^2\psi - \frac{\epsilon\mu^2}{a^2}\psi \quad (2.21)$$

where

$$\epsilon = \frac{4\Omega^2 a^2}{gH} = \left(\frac{a}{\sqrt{gH/2\Omega}} \right)^2 \quad (2.22)$$

is the Lamb's parameter. Equations (2.20) and (2.21) constitute the global version of shallow water quasi-geostrophic theory.

2.2.2 Validity of the Global SWQG Theory

It is impossible for us to calculate the geostrophy on the vicinity of the equator through geopotential distribution, since that if we recall the geostrophic divergence

$$\nabla \cdot \mathbf{u}_g = \frac{\partial\Phi}{\partial x} \frac{\partial(f^{-1})}{\partial y} = -v_g \cot\phi \frac{\partial\phi}{\partial y}, \quad (2.23)$$

we can find out the meridional geostrophic wind v_g should always equal to zero to avoid singularity; that is to say, there cannot be any mass accumulation on the equator, or the divergent would become infinite to smooth the height anomaly. The equator just serves as an impenetrable wall unable for waves to propagate through. Obviously, this is not the nature that we have observed in the tropics. The alternative method



is to express the wind field into partition of non-divergent and irrotational components, which can successfully avoid the computation of geostrophic velocities at and near the equator. We may be interested at the difference between geostrophic/ageostrophic wind and non-divergent/irrotational component.

The calculation starts from the geostrophic wind formula represented by stream field we obtained in (2.15). By applying the local linear balance condition $gh = f\psi$, the formula can be written as

$$\begin{aligned}(u_\psi, v_\psi) &= \left(-\frac{\partial\psi}{a\partial\phi}, \frac{1}{a\cos\phi} \frac{\partial\psi}{\partial\lambda} \right) \\ &= g \left(-\frac{\partial(h/f)}{a\partial\phi}, \frac{\partial(h/f)}{a\cos\phi} \frac{\partial}{\partial\lambda} \right).\end{aligned}\tag{2.24}$$

Since the Coriolis parameter does not change with longitude, the meridional wind component is simply

$$v_\psi = \frac{1}{a\cos\phi} \left(\frac{g}{f} \frac{\partial h}{\partial\lambda} \right) = v_g,\tag{2.25}$$

where v_g is the meridional geostrophic wind represented by perturbation height field in the spherical coordinate that we are familiar with. For u_ψ however, Coriolis parameter changes along the latitude and calculation yields

$$\begin{aligned}u_\psi &= -\left(\frac{g}{f} \frac{\partial h}{a\partial\phi} + \frac{gh}{a} \frac{\partial f^{-1}}{\partial\phi} \right) \\ &= -\frac{g}{f} \left(\frac{\partial h}{a\partial\phi} \right) - \frac{gh}{a} \frac{\partial(2\Omega\sin\phi)^{-1}}{\partial\phi} \\ &= u_g + \frac{1}{a} \frac{gh}{2\Omega\sin\phi} \cot\phi,\end{aligned}\tag{2.26}$$

where u_g is the zonal geostrophic wind represented by perturbation height field in

the spherical coordinate, with the extra term $\frac{1}{a} \frac{gh}{2\Omega \sin \phi} \cot \phi$. At most of the latitude, the Coriolis force changes slowly with latitude and the extra term is small as plotted in Fig. 1, which yields $u_\psi \approx u_g$; however, at the vicinity of the equator, this argument would not hold.

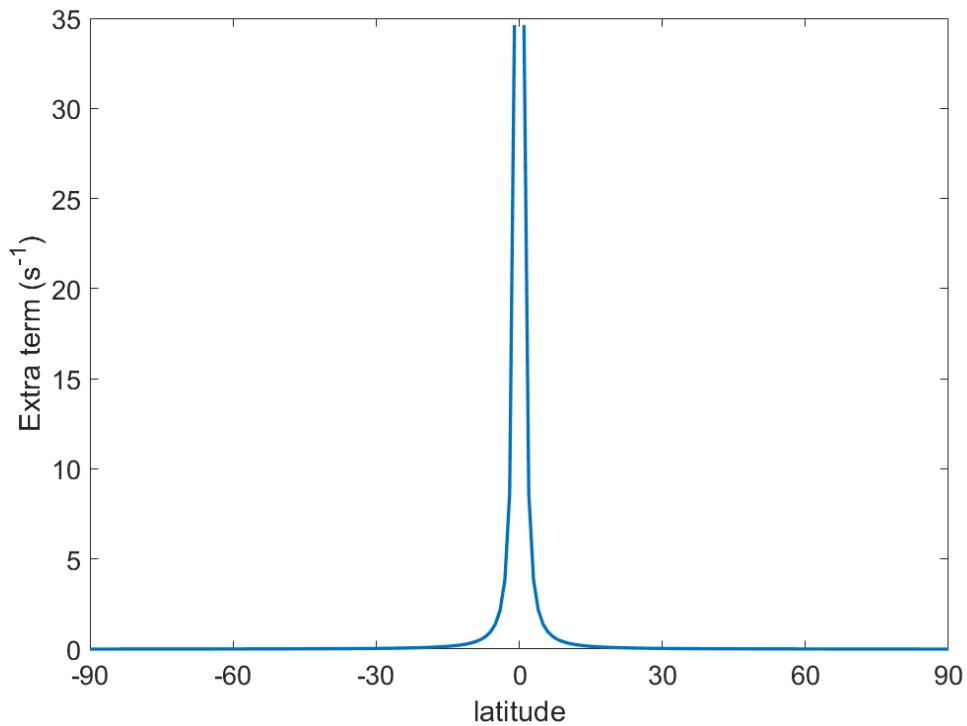


Figure 1. The extra term component $(2\Omega a \sin \phi)^{-1} g \cot \phi$ changing with latitude. We can see that at the vicinity of the equator, the component grows dramatically.

So, what is the physical meaning of the extra term? With the local linear balance condition, the zonal non-divergent wind component can be expressed as

$$u_\psi = u_g + \frac{\psi}{a} \cot \phi. \quad (2.27)$$

The divergence of the non-divergent wind is (of course zero. But here we still need to do some calculation and see what we would get)

$$\begin{aligned}
\nabla \cdot (u_\psi, v_\psi) &= \frac{\partial}{\partial x} \left(u_g + \frac{\psi}{a} \cot \phi \right) + \frac{\partial}{\partial y} v_g \\
&= \nabla \cdot (u_g, v_g) + \frac{1}{a} \frac{\partial \psi}{\partial x} \cot \phi \\
&= -\frac{1}{a} v_g \cot \phi + \frac{1}{a} v_\psi \cot \phi = 0 .
\end{aligned} \tag{2.28}$$

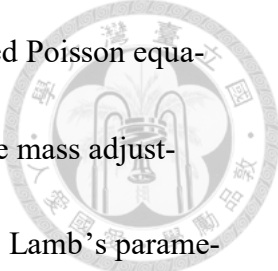


The divergence of the extra term had successfully cancelled out the geostrophic divergence, which means that the equator would not serve as a barrier for the transportation of potential vorticity. Also, if the motion has a smaller geostrophic meridional wind speed, we would expect the non-divergent motion to be more similar with the geostrophic motion. In chapter 3.3, we will show PV crossing the equator smoothly with this newly-built model and compare the height anomaly and PV anomaly field. The geostrophic wind and non-divergent wind actually have an enormous difference at the vicinity of equator. That is why Schubert *et al.* (2009) had mentioned that though it is called “quasi-geostrophic theory” in a general sense, the term “local linear balance theory” might be appropriate.

2.2.3 Physical Explanation

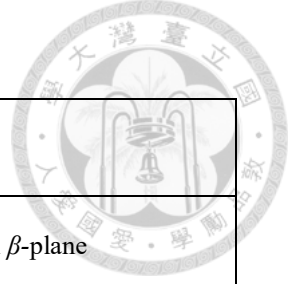
The primitive equations (2.12.1) ~ (2.12.3) have been reduced into two equation: the PV conservation relation (2.18), and the invertibility principle (2.19), forming a closed system. The PV conservation relation (2.18) consists of two parts: the nonlinear part $\frac{1}{a^2} \frac{\partial(\psi, q)}{\partial(\lambda, \mu)}$ which represents the advection, and the linear part $\frac{2\Omega}{a^2} \frac{\partial \psi}{\partial \lambda}$ which

produces Rossby wave. The invertibility principle (2.19) is a screened Poisson equation, including $\nabla^2\psi$ the non-divergent wind response and $\frac{\epsilon\mu^2}{a^2}\psi$ the mass adjustment. The only variable that controls the physical performance is the Lamb's parameter ϵ , which can be interpreted as the square of the ratio of the earth's radius to the Rossby radius of deformation. Since a , Ω and g are all constants, different magnitude of ϵ actually corresponds to different equilibrium height. Table 1 shows the equivalent depths and gravity wave speeds associated with different Lamb's parameter. The vertical modes transform (Fulton and Schubert, 1985) and the meaningful equivalent depths would be discussed in the next chapter. If $\epsilon = 0$, there would be no mass adaption and the model reduce to a non-divergent barotropic model. Different kinds of QGPV approach and formulas are listed in Table 2, and PV conservation equations are listed in Table 3 for comparison.



Modes	Equivalent Depth (m)	Gravity Wave Speed (ms ⁻¹)	Lamb's Parameter
External mode	~10000	~300	10
1 st internal mode	~300	~50	300
2 nd internal mode	~90	~30	1000

Table 1. Different vertical modes, the equivalent depths, gravity wave speeds associated with different Lamb's parameter.



$P = \nabla^2 \psi$	PV of non-divergent barotropic model
$P = \nabla^2 \psi + \beta y$	PV of non-divergent barotropic model on β -plane
$P = \nabla^2 \psi - \frac{1}{L_R^2} \psi$	SW-QGPV on f -plane
$P = \nabla^2 \psi - \frac{1}{L_R^2} \psi + \beta y$	SW-QGPV on β -plane
$P = \nabla^2 \psi - \frac{\epsilon \mu^2}{a^2} \psi + 2\Omega \mu$	SW-QGPV on the sphere

Table 2. Different kinds of potential vorticity anomaly. We can see SW-QGPV on the sphere having analogy to SW-QGPV on β -plane, except for the Coriolis force applied on the whole globe.

$\frac{\partial q}{\partial t} + \frac{\partial(\psi, q)}{\partial(x, y)} + \beta \frac{\partial \psi}{\partial x} = 0$	PV conservation principle on β -plane
$\frac{\partial q}{\partial t} + \frac{1}{a^2} \frac{\partial(\psi, q)}{\partial(x, y)} + \frac{2\Omega}{a^2} \frac{\partial \psi}{\partial x} = 0$	PV conservation principle on the globe

Table 3. PV conservation principles on the Cartesian coordinate and on the globe. The two equations are both consists of non-linear advection term and linear Rossby wave term.

2.2.4 Solution with Spheroidal Harmonics

The PV conservation principle is a non-linear equation, while the invertibility principle is linear and can be solved analytically using spheroidal harmonics. The spheroidal harmonics $S_{mn}(\epsilon; \lambda, \mu)$ form a complete set of orthogonal functions on the sphere, and would satisfy

$$\nabla^2 S_{mn} - \frac{\epsilon \mu^2}{a^2} S_{mn} = -\frac{\alpha_{mn}(\epsilon)}{a^2} S_{mn}, \quad (2.29)$$

where m is the zonal wave number, n is the total wave number and $-\frac{\alpha_{mn}(\epsilon)}{a^2}$ is the eigenvalue of the operator $\nabla^2 - \frac{\epsilon\mu^2}{a^2}$. We could separate the spheroidal harmonics to the meridional structures $S_{mn}(\epsilon; \mu)$ and the zonal structures in sinusoidal wave form

$$S_{mn}(\epsilon; \lambda, \mu) = S_{mn}(\epsilon; \mu)e^{im\lambda}, \quad (2.30)$$

substitute into (2.21), which yields the ordinary differential equation

$$\frac{d}{d\mu} \left[(1 - \mu^2) \frac{dS_{mn}}{d\mu} \right] + \left(\alpha_{mn} - \epsilon\mu^2 - \frac{m^2}{1 - \mu^2} \right) S_{mn} = 0. \quad (2.31)$$

This is the so-called “spheroidal wave equation”, and the eigenfunctions are the spheroidal wave functions $S_{mn}(\epsilon; \mu)$, while $\alpha_{mn}(\epsilon)$ are the eigenvalues of the spheroidal wave equation. Especially, when $\epsilon = 0$ representing a non-divergent barotropic model, the eigenvalues become independent of m and the solution reduces to spherical harmonics, i.e.

$$S_{mn}(0; \lambda, \mu) = P_{mn}(\mu)e^{im\lambda}, \quad (2.32)$$

$$P_{mn}(\mu) = (1 - \mu^2)^{\frac{m}{2}} \frac{d^m P_n(\mu)}{d\mu^m}, \quad (2.33)$$

where $P_n(\mu)$ denoting the ordinary Legendre polynomial. Fig. 2 shows the 3D plot of spherical harmonics and spheroidal harmonics with different wave numbers.

Noted that spherical harmonics can be solved analytically, while the spheroidal harmonics could only be solved numerically through transformation from spherical harmonics. Detailed introduction to spherical harmonics and the mathematical tech-

niques for calculating spheroidal harmonics would be shown in Appendix A. In practical, the Mathematica built-in functions *SpheroidalPS* and *SpheroidalPSPrime* are better tools to calculate the harmonics and their derivative. The codes of this model would be listed in Appendix B.

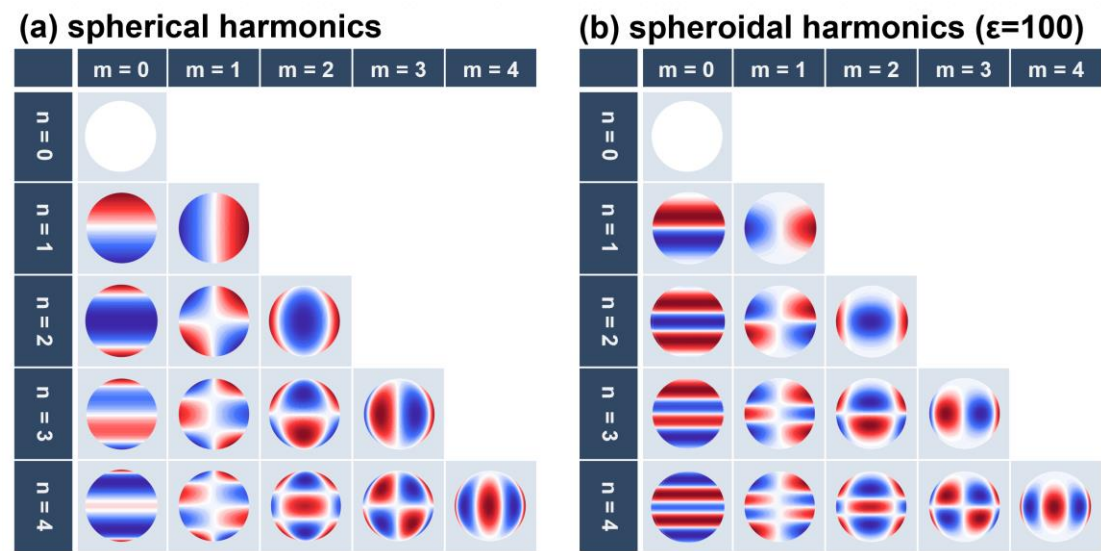
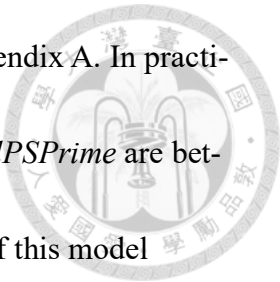


Figure 2. (a) Spherical harmonics and (b) Spheroidal harmonics ($\epsilon = 100$) with different wave numbers. The spheroidal harmonics looks just like the spherical harmonics being compressed on the zonal direction.

CHAPTER 3

The SW-QGPV Model on the Sphere



“I was particularly inspired by the concept of quasi-geostrophy and then fascinated by the fact that even highly simplified dynamical models such as the quasi-geostrophic barotropic model have some relevance to extremely complicated day-to-day weather changes.”

—— Akio Arakawa (2000)

3.1 Model Construction

The spheroidal harmonics should follow the orthonormality relation

$$\frac{1}{2} \int_{-1}^1 S_{mn}(\epsilon; \mu) S_{m'n'}^*(\epsilon; \mu) d\mu = \begin{cases} 1 & n' = n \\ 0 & n' \neq n. \end{cases} \quad (3.1)$$

where $S_{mn}^*(\epsilon; \mu)$ is the complex conjugate of $S_{mn}(\epsilon; \mu)$. Once we obtained the spheroidal wave functions $S_{mn}(\epsilon; \mu)$ in a discretized version from *SpheroidalPS*, we should normalize the functions and check the orthogonality through (3.1). After that, we can start to build our own model. The spheroidal harmonic transform pair for the PV anomaly is

$$q_{mn}(t) = \frac{1}{4\pi} \int_{-1}^1 \int_0^{2\pi} q(\lambda, \mu, t) S_{mn}^*(\epsilon; \lambda, \mu) d\lambda d\mu, \quad (3.2)$$

$$q(\lambda, \mu, t) = \sum_{m=-\infty}^{\infty} \sum_{n=|m|}^{\infty} q_{mn}(t) S_{mn}(\epsilon; \lambda, \mu). \quad (3.3)$$

where $S_{mn}(\epsilon; \lambda, \mu) = S_{mn}(\epsilon; \mu) e^{im\lambda}$. Also, substituting (3.3) into the invertibility principle (2.19) and (2.21) yields the invertibility principle in the spectrum space

$$\psi_{mn}(t) = -\frac{a^2 q_{mn}(t)}{\alpha_{mn}(\epsilon)}, \quad (3.4)$$

$$\psi(\lambda, \mu, t) = \sum_{m=-\infty}^{\infty} \sum_{n=|m|}^{\infty} \psi_{mn}(t) S_{mn}(\epsilon; \lambda, \mu). \quad (3.5)$$

Furthermore, the derivation on the meridional direction can also be obtained

$$\frac{dq(\lambda, \mu, t)}{d\mu} = \sum_{m=-\infty}^{\infty} \sum_{n=|m|}^{\infty} q_{mn}(t) DS_{mn}(\epsilon; \lambda, \mu), \quad (3.6)$$

$$\frac{d\psi(\lambda, \mu, t)}{d\mu} = \sum_{m=-\infty}^{\infty} \sum_{n=|m|}^{\infty} \psi_{mn}(t) DS_{mn}(\epsilon; \lambda, \mu). \quad (3.7)$$

where $DS_{mn}(\epsilon; \lambda, \mu) = \frac{dS_{mn}(\epsilon; \lambda, \mu)}{d\mu}$, could be calculated from *SpheroidalPSP*. We

should note that all these formulas are on the (λ, μ) coordinate, but not on the (λ, ϕ) coordinate and the transformation is needed.

The logic of this generalized spectrum model is rather easy. If the initial PV anomaly distribution $q(\lambda, \phi, t_0)$ is known, we may transform it to $q(\lambda, \mu, t_0)$ through interpolation. Using (3.2) helps us to obtain the components of PV anomaly $q_{mn}(t_0)$ in the spectrum space, while the components of flow field $\psi_{mn}(t_0)$ from (3.4). The

zonal derivation $\frac{dq(\lambda, \mu, t_0)}{d\lambda}$ and $\frac{d\psi(\lambda, \mu, t_0)}{d\lambda}$ can be derived from FFT, while obtaining

$\frac{dq(\lambda, \mu, t_0)}{d\mu}$ and $\frac{d\psi(\lambda, \mu, t_0)}{d\mu}$ should apply (3.6) and (3.7). The PV conservation principle



(2.18) then can be computed in the physical space to predict the evolution of PV anomaly. The complete spheroidal-based model in this research is written in Matlab, and the codes are shown in Appendix B. The space resolution is 240×121 grids, with cutoff wavenumber to be 80 and the time resolution is 0.25 hour per step, using RK4 time integration. Fig. 3 shows the flow chart for solving this model. Fig. 4 shows the difference between (λ, ϕ) and (λ, μ) coordinates with the grids. We should note that more grids are used to describe the low latitude area on the (λ, μ) coordinate, while less grids are for the high latitude and may cause larger error when calculating fields near the pole.

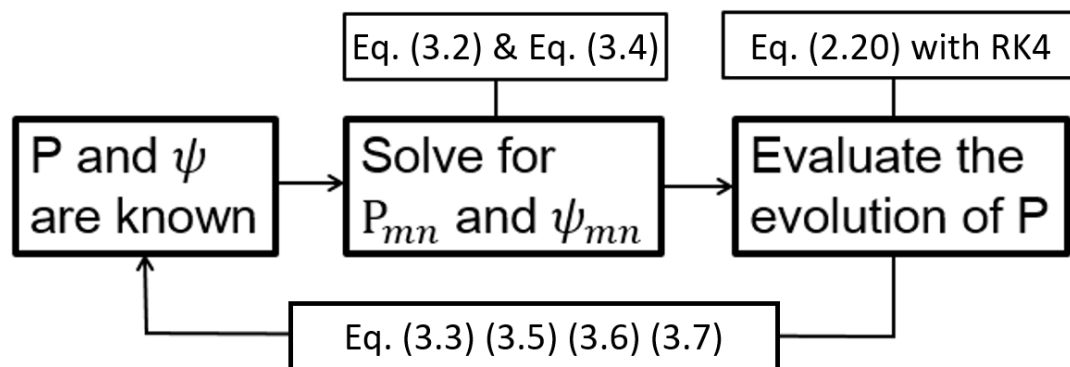


Figure 3. The flow chart for solving the spheroidal harmonic based global SWQG model.

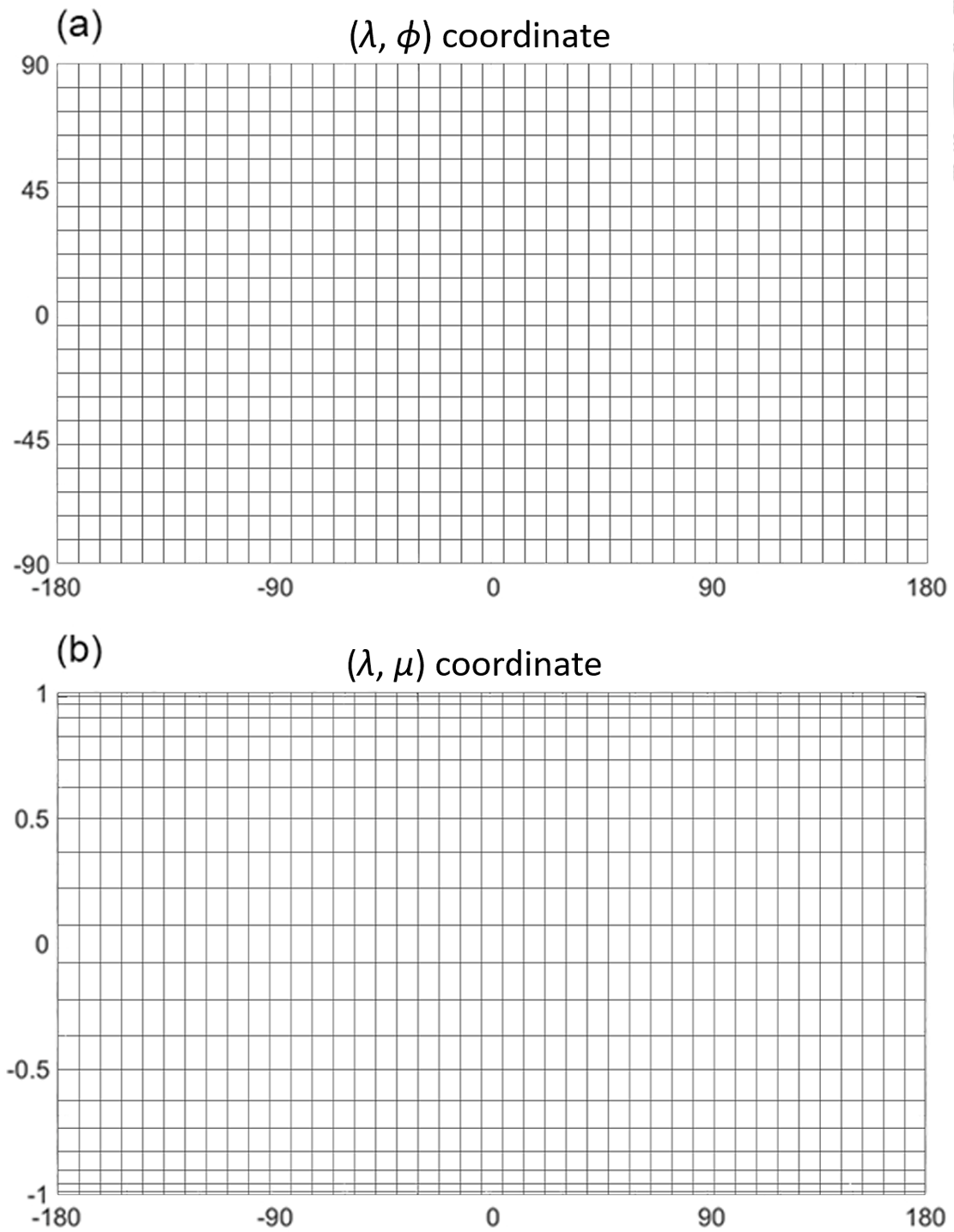


Figure 4. The grid points on (a) (λ, ϕ) coordinate and (b) (λ, μ) coordinate. We should notice that on the area at high latitude is compressed, while area at the low latitude is stretched on the (λ, μ) coordinate.

3.3 Model Performance

3.3.1 Invertibility Principle

Starting from the analysis of a 1-dimensional screened Poisson equation

$$(\nabla^2 - \gamma^2) \psi(x) = q(x), \quad (3.8)$$

let $\psi = \hat{\psi}e^{ikx}$, $q = \hat{q}e^{ikx}$ and transform the equation into spectrum space

$$-(k^2 + \gamma^2) \hat{\psi} = \hat{q}. \quad (3.9)$$

We can obtain the components of each terms through linear combinations

$$\begin{aligned} \nabla^2 \hat{\psi} &= \frac{k^2}{(k^2 + \gamma^2)} \hat{q}, \\ -\gamma^2 \hat{\psi} &= \frac{\gamma^2}{(k^2 + \gamma^2)} \hat{q}. \end{aligned} \quad (3.10)$$

Mathematically speaking, γ behaves as the strength of the screening. When γ is small, the solution approaches the unscreened Poisson equation; on the other hand, when γ is extremely large, ψ approaches the value q/γ^2 , which goes to zero as γ goes to infinity. The analytical solution of an appropriate γ requires the Green's function and would not be shown here, but we would expect that larger γ would decrease the magnitude of ψ and make the $\psi - q$ relation more linear with a fixed q .

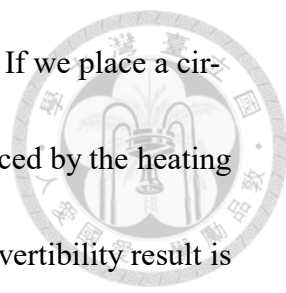
Back to the invertibility principle (2.21), the components can be written as

$$\begin{aligned} \nabla^2 \hat{\psi} &= \frac{k^2}{(k^2 + 1/L_d^2)} \hat{q}, \\ -\left(\frac{1}{L_d^2}\right) \hat{\psi} &= \frac{1/L_d^2}{(k^2 + 1/L_d^2)} \hat{q}, \end{aligned} \quad (3.11)$$



where $1/L_d^2 = \epsilon\mu^2/a^2$. The behaviors of the equations become clear. If the mass response is large, which corresponds to the higher latitude, higher rotation speed, or lower gravity wave speed, we would expect that the streamfunction ψ becomes smaller and the contour of ψ becomes more parallel to the contour of q . The PV invertibility results of an elliptical Gaussian shape PV anomaly placing at 45°N with the non-divergent barotropic model ($\epsilon = 0$) and global SWQG model with $\epsilon = 300$ (SWQG_E300) is shown in fig. 5 for comparison. The magnitude of the PV anomaly is set to be $-1 \times 10^{-5} \text{s}^{-1}$ at the center.

We can also obtain the information of the mass and velocity field through the streamfunction distribution by local linear balance condition (2.19). By doing so, we could check the difference between geostrophic wind and non-divergent wind, as mentioned in section 2.2.2. We may place a circular Gaussian shape of PV anomaly at 45°N to SWQG_E300, with magnitude $-1 \times 10^{-5} \text{s}^{-1}$ placing at the center. As we can see in fig. 6, the contour of streamfunction and the contour of height anomaly is more parallel at high latitude. Meridional components of non-divergent wind and geostrophic wind is the same. Zonal components of the geostrophic wind have some difference from the non-divergent wind at lower latitudes due to (2.26), but still the pattern is similar.



Situation becomes weird when PV anomaly is near the tropics. If we place a circular gaussian shape heating above the equator, the PV forcing induced by the heating is $DP/Dt \propto f$, and would be anti-symmetric to the equator. The invertibility result is shown in fig 7. We can see that the height anomaly is symmetric to the equator. There exists strong zonal geostrophic winds near the equator, but is 50% weaker at the non-divergent wind pattern. We should notice that in this situation, the traditional quasi-geostrophic theory actually breaks down since the Rossby number is not small enough, and the geostrophic wind we obtained may not be consistent with the observation. The meridional component of geostrophic wind and non-divergent wind remains the same, except the singularity at the equator. Cancelling out the over-estimating of geostrophic wind is the key point of this model to allow PV penetrate through the equator without singularity.

3.3.2 Linear Rossby Wave Propagation

The global SWQG model may not be a good tool for analyzing the tropical weather systems since it contains only PV dynamics. Important mechanisms such as Kelvin waves could not be obtained from this model. However, this model gives us an alternative method for simulating PV propagating over the equator and gives us a thorough insight when the motion is guided by PV dynamics. One of the examples is the linear Rossby wave propagation.

The linear Rossby wave is governed by the linearized version of (2.20)

$$\frac{\partial q}{\partial t} + \frac{2\Omega}{a^2} \frac{\partial \psi}{\partial \lambda} = 0. \quad (3.12)$$

Plugging the spectrum version of invertibility principle (2.29), we can obtain

$$q(\lambda, \mu, t) = \left(\frac{2\alpha_{mn}(\epsilon)}{a^2} \right)^{\frac{1}{2}} S_{mn}(\epsilon; \mu) e^{[im\lambda + v_{mn}(\epsilon)t]}, \quad (3.13)$$

and

$$\psi(\lambda, \mu, t) = - \left(\frac{2a^2}{\alpha_{mn}(\epsilon)} \right)^{\frac{1}{2}} S_{mn}(\epsilon; \mu) e^{[im\lambda + v_{mn}(\epsilon)t]}, \quad (3.13)$$

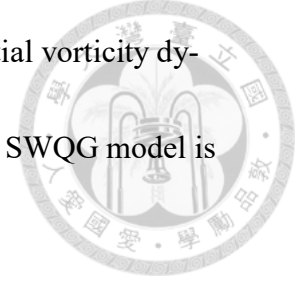
where

$$v_{mn}(\epsilon) = \frac{2\Omega m}{\alpha_{mn}(\epsilon)}. \quad (3.14)$$

Schubert et al. (2009) had compared the frequencies with the solution obtained from shallow water primitive equations numerically, computed by Longuet-Higgins (1968).

Their article indicated that quasi-geostrophic Rossby wave frequencies (3.14) are very good approximations to the primitive equation frequencies, with the exception of low zonal wavenumber sectoral harmonics, i.e., small $|m|$ for $n - |m| = 0$. For example, in the case $\epsilon = 10$, the largest errors are for $n = m = 1$ (34% error) and $n = m = 2$ (9.9% error). They proposed two reasons: one is that the low zonal wavenumber sectoral harmonics have h and ψ fields vary as slowly as $2\Omega\mu$, so that the assumptions of local linear balance relation (2.19) begin to break down. The second reason is that primitive

equation model can capture both gravity wave dynamics and potential vorticity dynamics in the low zonal wavenumber sectoral harmonics, while the SWQG model is only able to capture the potential vorticity part of the dynamics.



We would be interested about how the Rossby wave frequencies varies with different ϵ , and what is the difference between the complete barotropic model and the non-divergent barotropic model, which was often used in the very early days of numerical weather prediction. Since that the Rossby wave frequency of the non-divergent barotropic model can be written as

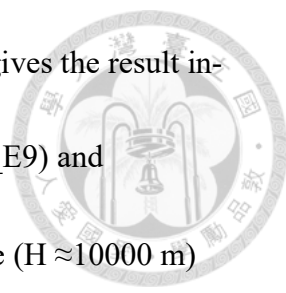
$$v_{mn}(0) = \frac{2\Omega m}{n(n+1)}, \quad (3.15)$$

the Rossby wave frequency of the complete barotropic model can be rewritten as

$$v_{mn}(\epsilon) = \frac{n(n+1)}{\alpha_{mn}(\epsilon)} \frac{2\Omega m}{n(n+1)} = C \times v_{mn}(0), \quad (3.16)$$

where C is defined as the correction factor. Without correction factor, the non-divergent barotropic model would produce an erroneous westward propagation of ultralong waves. The correction factor with different wave numbers produced by Schubert *et al.* (2009) is shown in fig 8. Longer waves and larger ϵ would increase the correction factor, which means that it would cause larger error when using non-divergent barotropic model.

To see how the model really works, an initial value problem is to put a circular Gaussian shape PV anomaly at 30 °N with the magnitude of $-2.5 \times 10^{-5} s^{-1}$ at the



center, without non-linear effect and background mean flow. Fig 9 gives the result integrated for 10 days with global SWQG model with $\varepsilon = 9$ (SWQG_E9) and SWQG_E300. Remind that SWQG_E9 stands for the external mode ($H \approx 10000$ m) and SWQG_E300 stands for the first internal mode ($H \approx 300$ m) under vertical transformation. We can see that PV anomaly successfully penetrate the equator in both model, which is not able to achieve in the classical QG approach. Rossby wave dispersion can be clearly observed. The dispersion is faster in the SWQG_E9 case, and also the PV anomaly is wide spread on the globe. For SWQG_E300 case, however, the propagation of PV anomaly is constrained in the mid-latitudes and the tropical area. For height anomaly, we can see that there is no mass adaption at the vicinity of the equator, and most of the anomalies are at mid-latitudes. Negative PV represents positive height anomaly at the northern hemisphere, while it yields negative height anomaly at the southern hemisphere, due to the anti-symmetry of the Coriolis force to the equator.

The two models explained two different regimes of physics. We may use the SWQG_E9 model to explore tele-connection due to topography and forcing, while using SWQG_E300 model to diagnose the PV dynamics of cumulus heating. We should choose a appropriate model before we start our scientific experiments.

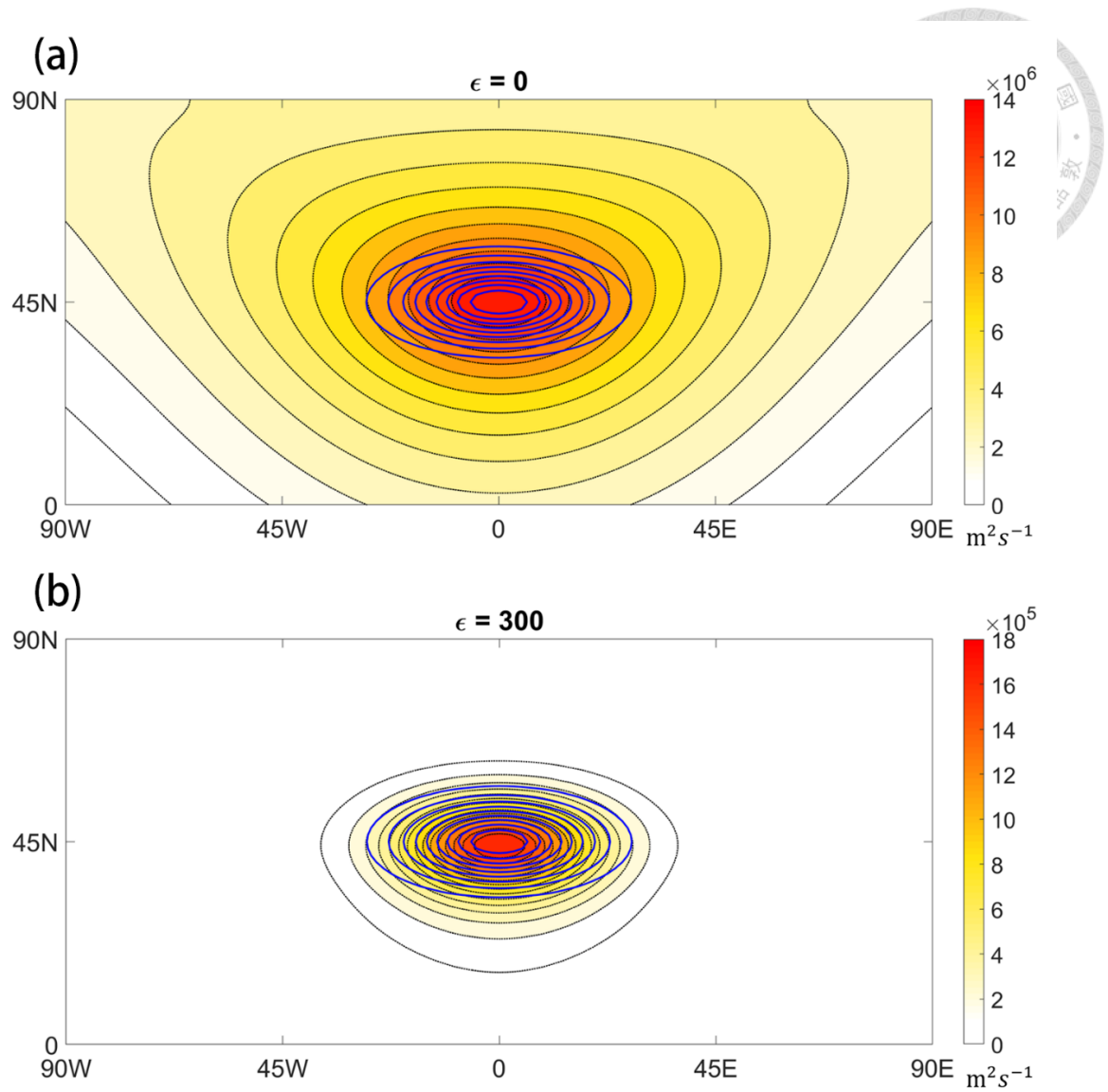


Figure 5. The elliptical PV anomaly located at 45 °N (dotted thick contour, in s^{-1}) and its streamfunction (shading, in m^2s^{-1}) of (a) non-divergent barotropic model and (b) SWQG_E300. We can see that with a stronger mass response (the stronger screened effect), the streamfunction becomes smaller, localized, and its contour becomes more parallel to the contour of the PV anomaly.

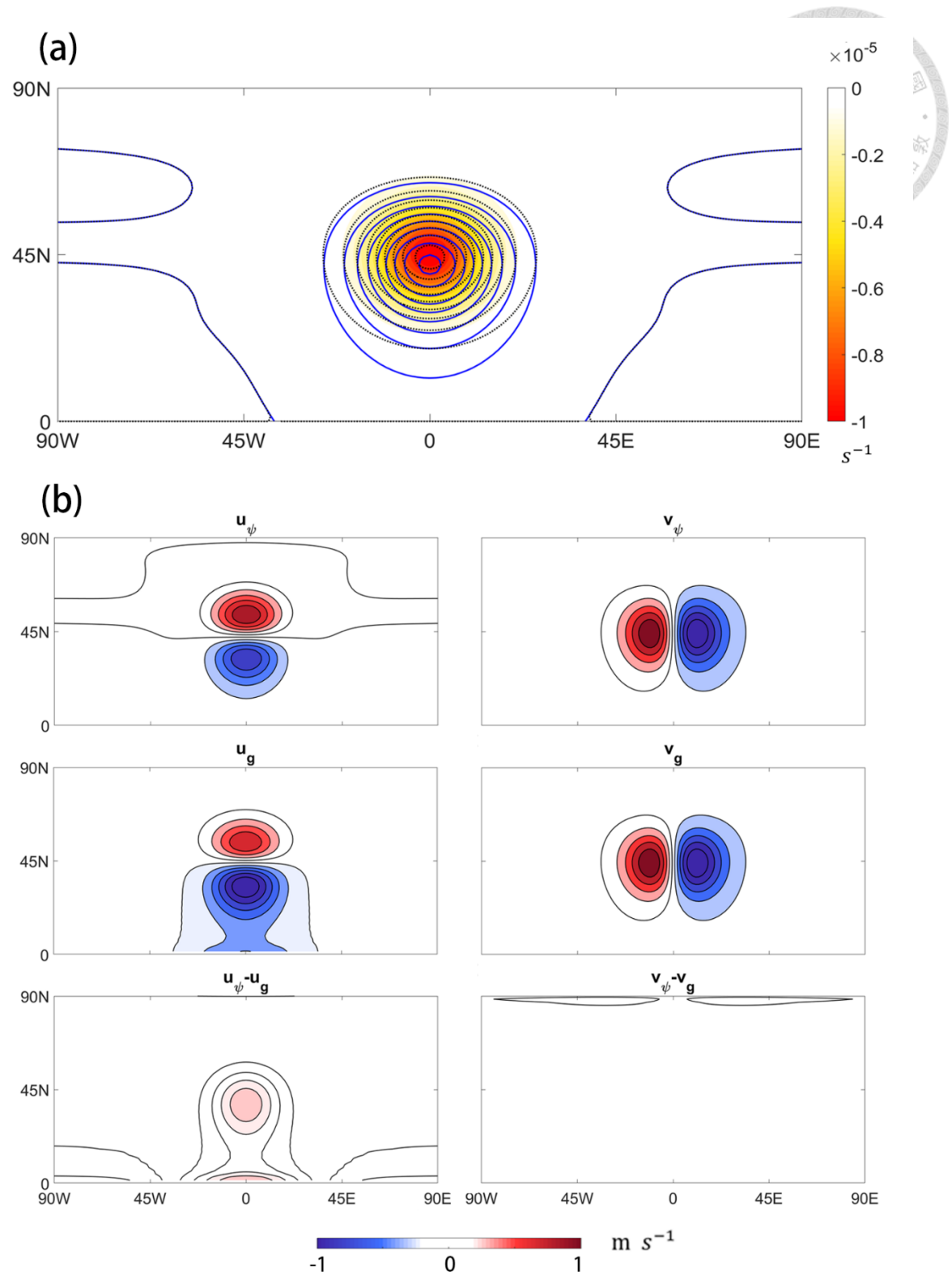


Figure 6. (a) The circular PV anomaly located at 45 °N (shading, in s^{-1}), its streamfunction (blue dotted contour, in m^2s^{-1}), and its height anomaly (black contour, in m) under SWQG_E300. (b) Left: the zonal component of the non-divergent wind, geostrophic wind, and their difference from top to bottom. Right: same as the left but for the meridional component.

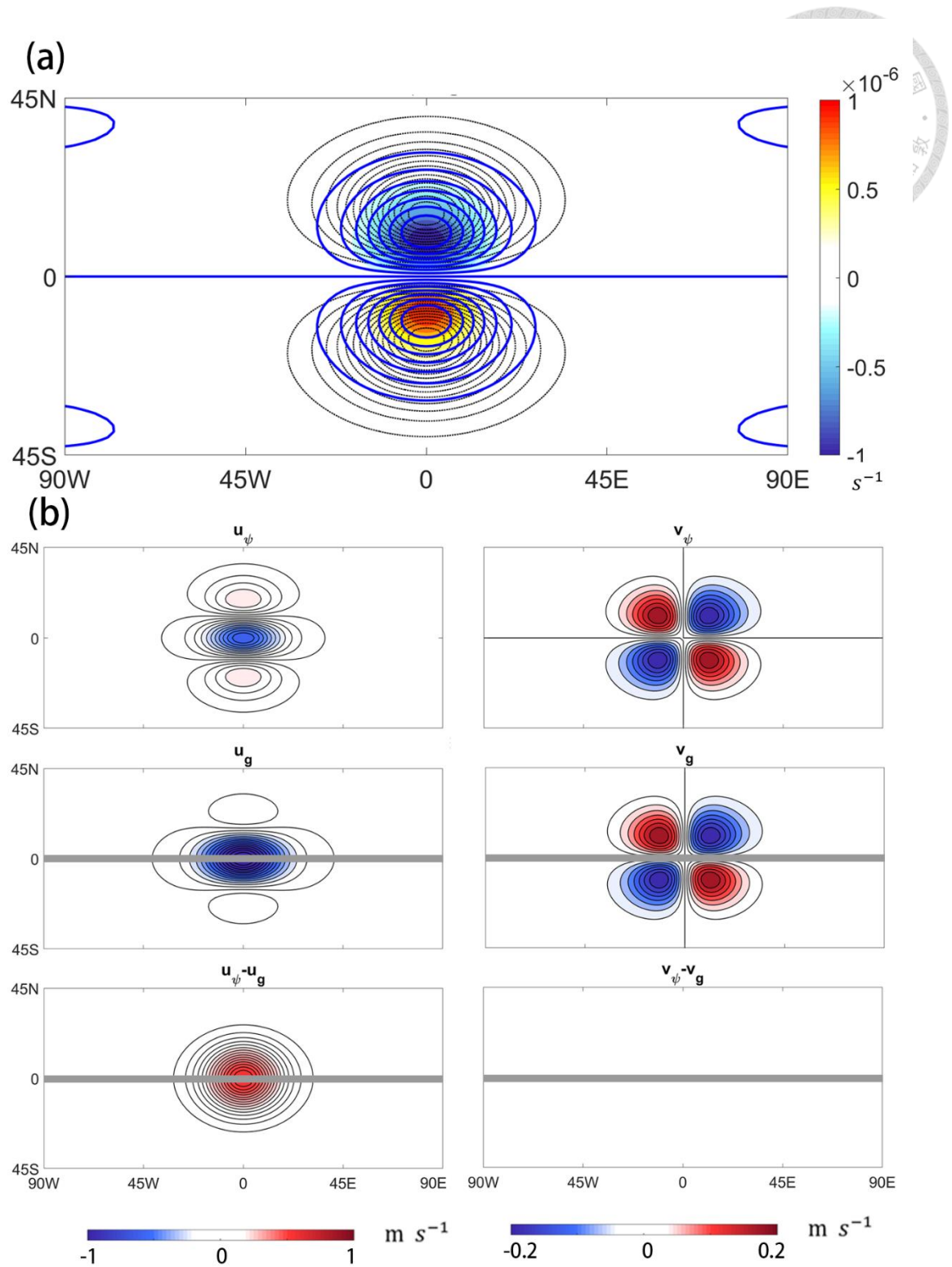


Figure 7. (a) The PV anomaly caused by heating located at the equator (shading, in s^{-1}), its streamfunction (blue dotted contour, in $m^2 s^{-1}$), and its height anomaly (black contour, in m) under SWQG_E300. (b) Left: the zonal component of the non-divergent wind, geostrophic wind, and their difference from top to bottom. Right: same as the left but for the meridional component.

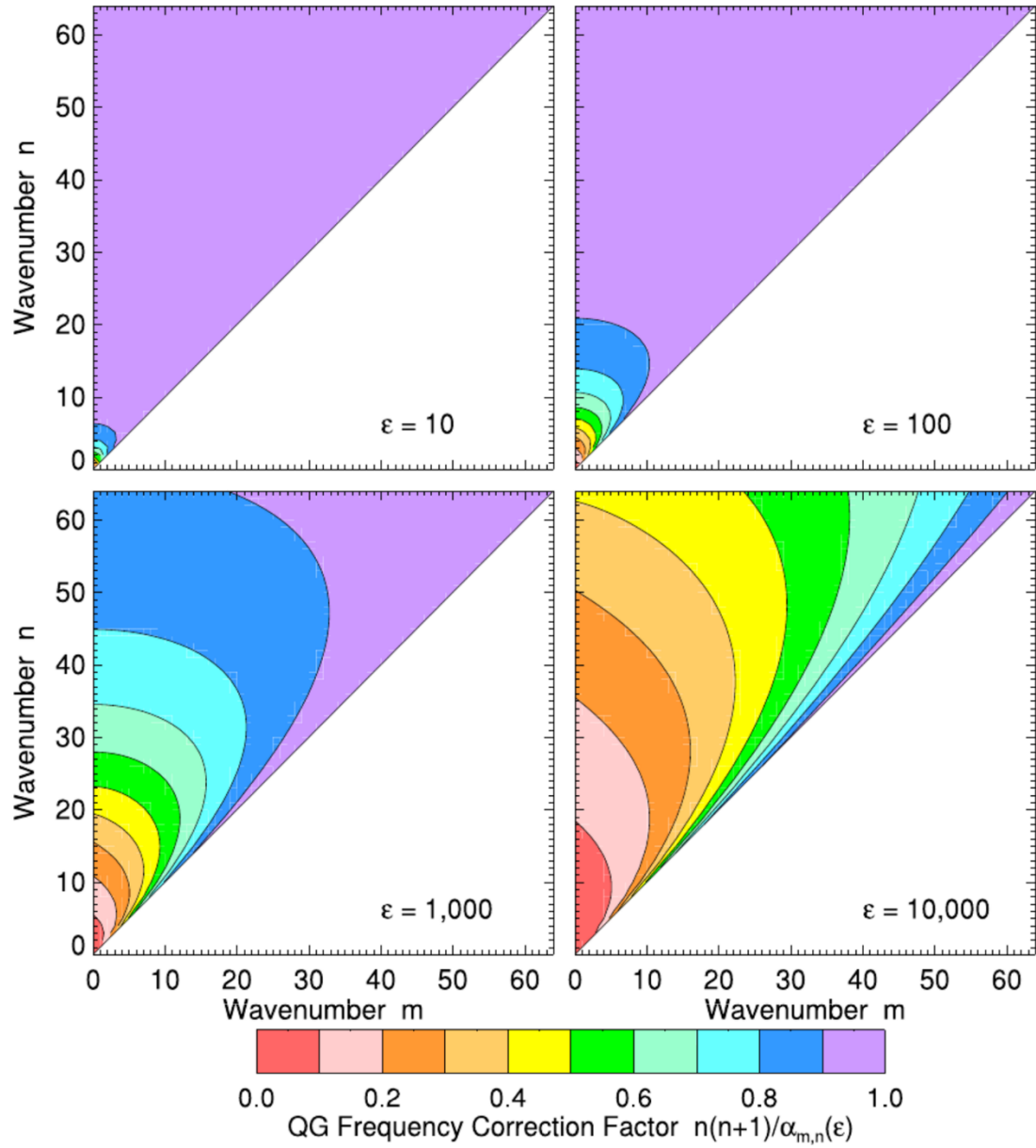


Figure 8. Isolines of the “quasi-geostrophic frequency correction factor” for $\varepsilon = 10, 100, 1000$ and 10000 . Adapted from Schubert *et al.* (2009).

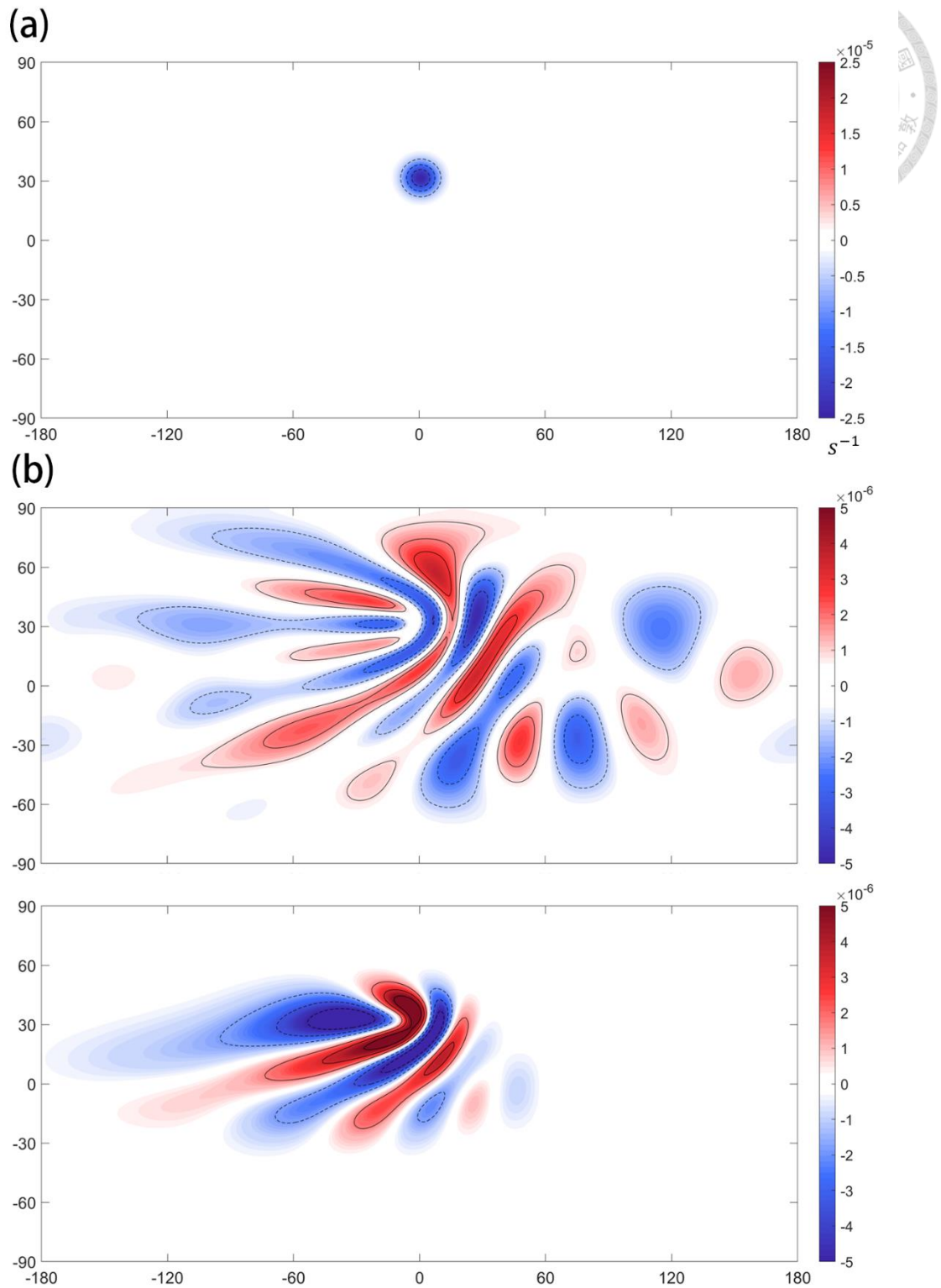


Figure 9. (a) The initial circular PV anomaly located at 30 °N (shading, in s^{-1}). (b) Upper: PV anomaly after 10 days of integration under SWQG_E9. Down: PV anomaly after 10 days of integration under SWQG_E300. (c) Same as (b), but for height anomaly.

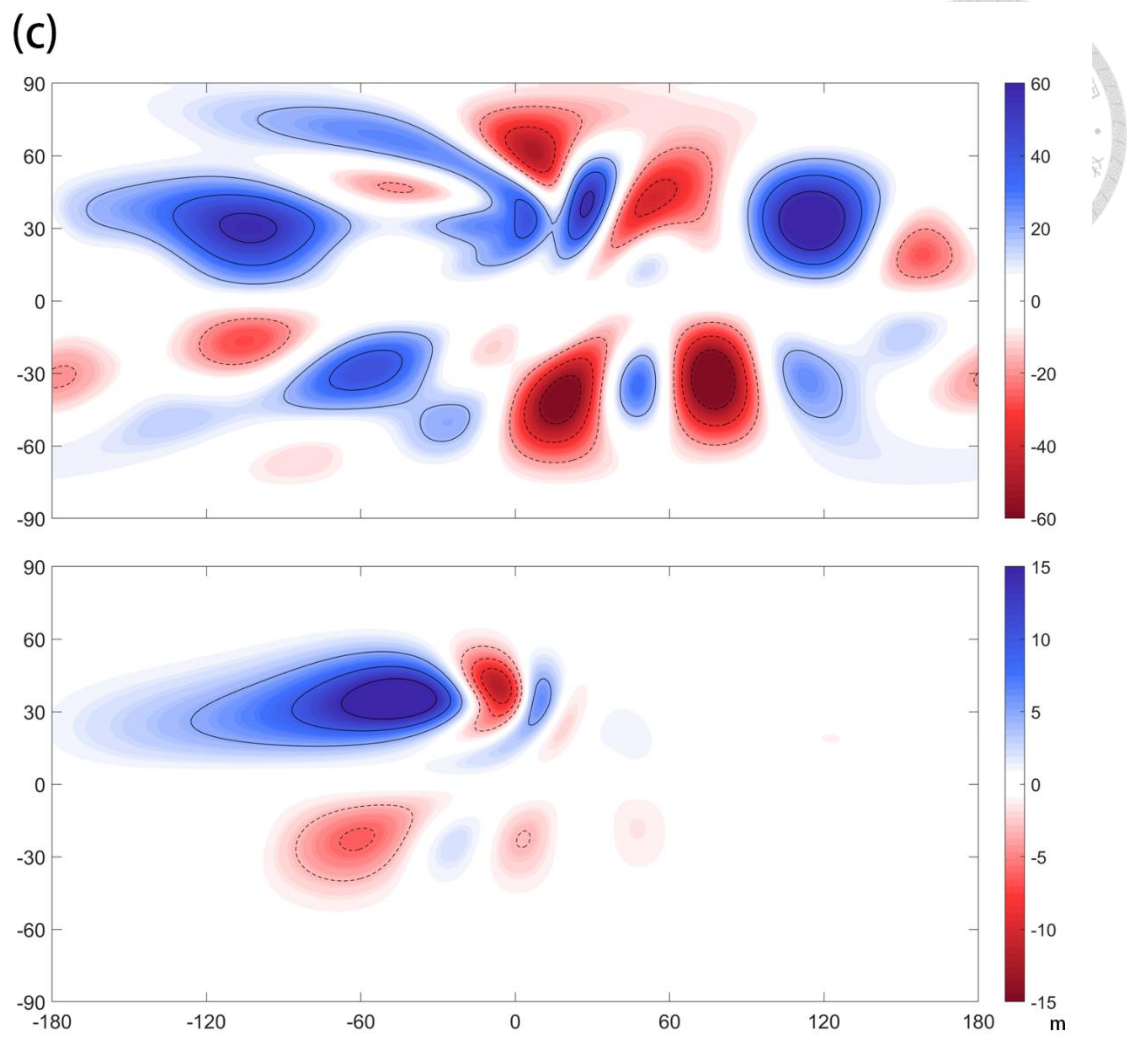


Figure 9. (continued)

3.4 Model with Topography



We can derive the global SWQG theory with topography in a rather easy way, which is not mentioned in the early research. We may rewrite the potential vorticity equation (2.14) with topography

$$\begin{aligned} P &= \left(\frac{H}{H+h-\eta} \right) \left(2\Omega \sin\phi + \left(\frac{\partial v}{a \cos\phi \partial \lambda} - \frac{\partial(u \cos\phi)}{a \cos\phi \partial \phi} \right) \right) \\ &= \left(\frac{H}{H+h-\eta} \right) (f + \nabla^2 \psi), \end{aligned} \quad (3.17)$$

where $f = 2\Omega \sin\phi$ and $\nabla^2 \psi = \left(\frac{\partial v}{a \cos\phi \partial \lambda} - \frac{\partial(u \cos\phi)}{a \cos\phi \partial \phi} \right)$. We assume that the height anomaly and topography is small enough, which means that $(h - \eta) = \epsilon \ll H$. Equation (3.17) can be rewritten as

$$\begin{aligned} P &= \left(\frac{H}{H+\epsilon} \right) (f + \nabla^2 \psi) \\ &\approx f + \zeta - f \frac{h}{H} + f \frac{b}{H} - \zeta \frac{h}{H} - \zeta \frac{b}{H} \\ &\approx f + \zeta - f \frac{h}{H} + f \frac{b}{H} = f + q. \end{aligned} \quad (3.18)$$

The last approximation requires ζ to be relatively small comparing to f . PV anomaly then can be written as

$$q = \nabla^2 \psi - \frac{\epsilon \mu^2}{a^2} \psi + 2\Omega \mu \frac{b}{H} \quad (3.18)$$

With this result, we can revisit the classical experiment conducted by Grose and Hoskins (1979), about the over-rotating flow over topography. The over-rotating flow is 15 ms^{-1} multiplying cosine of the latitude, and the mountain is set to be a circular gaussian function located at 30°N , with the maximum height to be 2500 m, and the

model used here is SWQG_E9. The original paper placed an elliptical sinusoidal shape mountain with eccentricity of 0.5 and used the linearized one-layer shallow water model. The result is shown in fig 10 and fig 11. We could see the stationary

Rossby wave result is reproduced with very similar patterns.

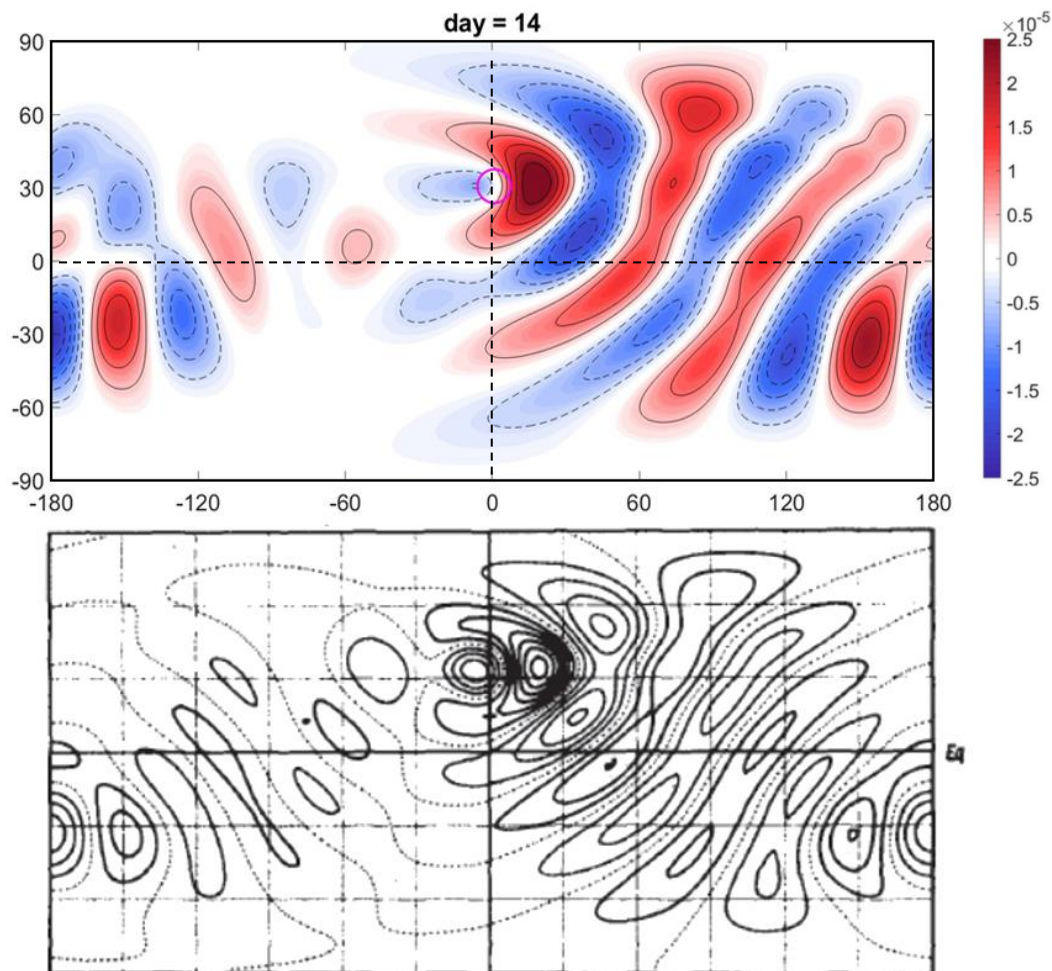
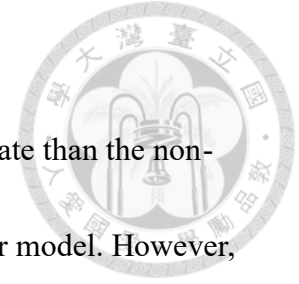


Figure 10. Upper: the PV anomaly (shading, in s^{-1}) of the super-rotational flow experiment with topography (circled with magenta), conducted with SWQG_E9. Below: the original result from Grose and Hoskins (1979), where contour is the vorticity anomaly. Note that PV anomaly and vorticity anomaly are almost the same in the external mode, due to lack of mass response.

3.5 Usage of the global SWGQ model



This model serves as an intermediate model that is more accurate than the non-divergent barotropic model, but less accurate than the shallow water model. However, if the system we are interested about is a synoptic scale system with lower wave-number, this model could successfully filter out the high wave number dynamics (i.e. gravity waves) while preserving the low wave number dynamics and mass distribution. With less computation cost, this model could be a great tool for pedagogical and diagnose usage. A possible usage of this model is dealing with system that are located on the subtropics, spanning from the midlatitudes with strong Coriolis effect, to the tropics without Coriolis force. β -plane approximation would be not good enough, and the strength of mass response differs with latitude. We will show how to diagnose this kind of system – the South Asian High, in the next chapter.

CHAPTER 4

The PV perspective of South Asian High



4.1 Introduction and Methodology

South Asian high (SAH) is an upper-tropospheric anticyclonic system, elongating from east Asia to Sahara Desert in boreal summer, as shown in fig 12 (a) on the geopotential height map. It is well recognized that the Tibetan plateau (TP) exerts intense and persistent diabatic heating, both sensible heat flux and latent heat release, to the atmosphere and gives rise to the formation and maintenance of SAH. (He et al., 1987; Yanai and Lee, 1994; Liu et al., 2001; Duan et al., 2005). SAH plays an important role on global climate circulation, including the onset and persistent of East Asian summer monsoon (EASM), the formation of tropical upper tropospheric trough (TUTT), etc. On the other hand, originating from the East Asia, this thermally driven circulation may affect the subsidence over the Mediterranean and the Sahara Desert, which is the monsoon-desert coupling mechanism proposed by Rodwell and Hoskins (1996; 2001) under the linear dynamic regime. This phenomenon indicates that there might be a teleconnection between EASM and the drought of Mediterranean during summer.

PV anomaly could also be observed on the isentropic PV (IPV) map near the tropopause. As mentioned in the previous chapter, PV contains both mass and velocity

field and is useful for synoptic scale weather diagnosis. However, there are less analysis on SAH that uses PV as the tool. In this chapter, we will introduce the PV perspective of the SAH. The data used in this study including the hourly/monthly ECMWF Reanalysis v5 (ERA5) data on pressure level at a resolution of $2.5^\circ \times 2.5^\circ$ and ERA5 precipitation data on land at a resolution of $1.25^\circ \times 1.25^\circ$. The research period covers the boreal summer seasons (from June to August, JJA) from 1979 to 2020. Geopotential height on 150 hPa isobaric surface and IPV at 370 K isentropic surface are chosen as the level for investigation of SAH. Fig. 12 shows the July mean geopotential and IPV map of SAH.

4.2 The Heating Structure of SAH

We may calculate the horizontal and vertical heating structures following the equations below (Yanai *et al.*, 1973):

$$Q_1 = c_p \left(\frac{p}{p_0} \right)^\kappa \left[\frac{\partial \theta}{\partial t} + \mathbf{v} \cdot \nabla \theta + \omega \frac{\partial \theta}{\partial p} \right], \quad (4.1.1)$$

$$Q_2 = -L \left[\frac{\partial q}{\partial t} + \mathbf{v} \cdot \nabla q + \omega \frac{\partial q}{\partial p} \right], \quad (4.1.2)$$

where θ is the potential temperature, q the mixing ratio of water vapor, \mathbf{v} the horizontal velocity, ω the p-velocity, p the pressure. $\kappa = 0.286$, $p_0 = 1000$ hPa, and L the latent heat of condensation. Q_1 is defined as the apparent heat source, while Q_2 the apparent moisture sink. Integrating (4.1.1) and (4.1.2) from the top and bottom of the layer yields

$$\langle Q_1 \rangle = \frac{1}{g} \int_{p_b}^{p_t} Q_1 dp = \langle Q_R \rangle + LP + S, \quad (4.2.1)$$

$$\langle Q_2 \rangle = \frac{1}{g} \int_{p_b}^{p_t} Q_2 dp = L(P - E), \quad (4.2.2)$$

where p_t and p_b are the pressure of top and bottom boundary, $\langle Q_R \rangle$ is the integrated radiative heating rate, and P, S, E are respectively the precipitation rate, the sensible heat flux and the evaporation rate per unit area at the surface. We should note that

$$\langle Q_1 \rangle - \langle Q_2 \rangle = \langle Q_R \rangle + S + LE. \quad (4.3)$$

Careful comparison between the distributions of Q_1 and Q_2 will yield valuable information on the nature of heating processes. The heating structure of July over TP (27°–37°N, 80°–100°E) and Yangzi River (YR) valley (28°–33°N, 100°–120°E) is calculated, as shown in fig. 13 (a) and (b). We could see Q_2 is only a quarter of Q_1 over TP, which means that radiation heating and sensible heat flux is the main heating source over the plateau. Above YR valley, the maximum value of Q_2 is almost the same as Q_1 , which indicates that condensational heating is the dominant factor heating the atmosphere of the EASM area. The maximum heating rate over YR region is about 3 K/day and TP region is about 4 K/day at 400–500 hPa. The outcomes are consistent with the analysis done by Nita (1977) and Yanai *et al.* (1994).

Needs to notice that heating over YR valley varies with the precipitation and had a big variability. For the dramatic rainfall event during 2020, the July monthly mean heating rate is about 6 K/day (fig. 13 (c)).



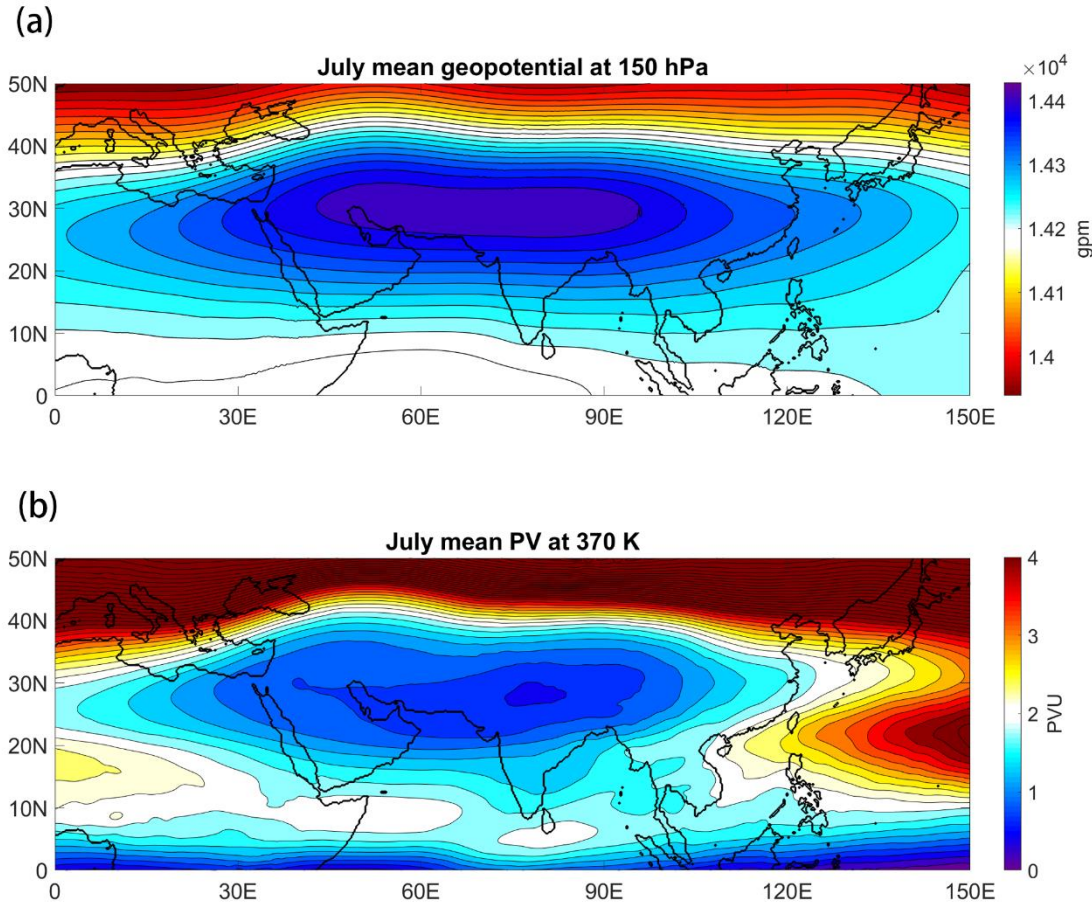


Figure 12. The July mean (a) geopotential height (shading, in gpm) and (b) PV (shading, in PVU) of the SAH, averaged from 1979 to 2020.

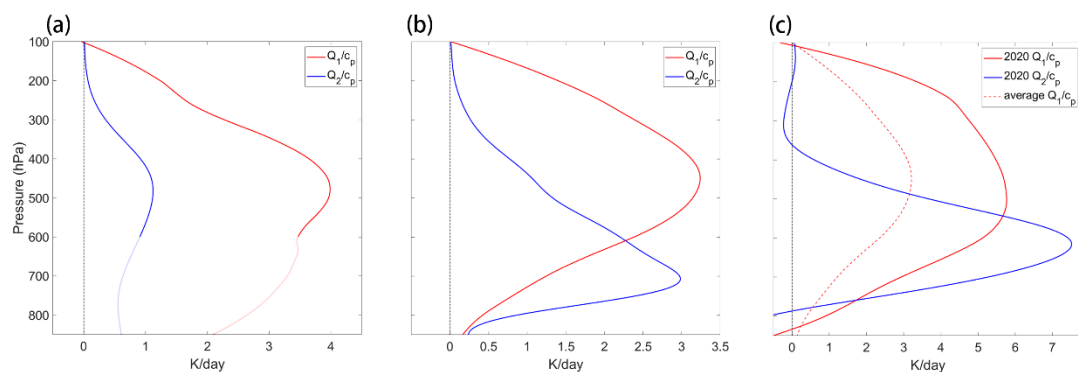
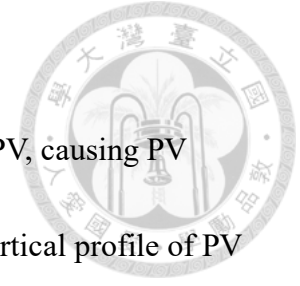


Figure 13. The July monthly mean vertical distribution of the apparent heating rate Q_1/c_p (red) and the moist heating rate Q_2/c_p (blue) for (a) Tibetan Plateau, averaged from 1979 to 2020, (b) Yangtze River valley, averaged from 1979 to 2020, and (c) Yangtze River valley at 2020, with red dotted line to be 42-year averaged Q_1/c_p for comparison. Heating structure of TP below 600 hPa are below the ground and may not be realistic.

4.3 The PV forcing of SAH



Thermal forcing transfers mass and would concentrate/dilute PV, causing PV forcing between two isentropes. Fig. 14 (a) shows the July mean vertical profile of PV and potential temperature at 30 °N. We can see isentropes bent to the ground, with negative PV anomaly produced between 350K and 380K isentropes. Fig. 14 (b) are the schematic diagrams of this mechanism. For the northern hemisphere, mass is transported into the two isentropes, diluting the positive PV, and producing negative PV anomaly.

PV forcing caused by heating on the isentropic coordinate can be formulated in the form of (Hoskins et al., 1985)

$$\frac{dP}{dt} \approx -\sigma^{-1}(f + \zeta_{\theta}) \frac{\partial \dot{\theta}}{\partial \theta} , \quad (4.4)$$

where P is the potential vorticity, ζ the relative vorticity, θ the potential temperature and $\sigma = -\frac{1}{g} \frac{\partial p}{\partial \theta}$ defined as the isentropic density. $\dot{\theta}$, the heating rate, can be obtained from (4.1.1) and (4.2.1), choosing $p_t = 100\text{hPa}$ and $p_b = 300\text{hPa}$. This formula is derived with the assumptions of small Rossby number, small Richardson number, and lack of friction. Fig. 14 (c) is the schematic diagram of PV forcing calculation using this formula. Heating at the middle of the troposphere would cause negative PV anomaly at the upper troposphere and positive PV anomaly at the lower troposphere.

Fig. 15 (a) shows the PV forcing map at the vicinity of SAH. East and west of the

SAH are negative PV source and sink, respectively. Above TP and YR region, the forcing is nearly - 1.5 PVU/day. Also, the monthly mean precipitation is presented in fig. 15 (b) to specify the correspondence between PV forcing and precipitation. We can observe that the precipitation pattern fits the location of negative PV source well.

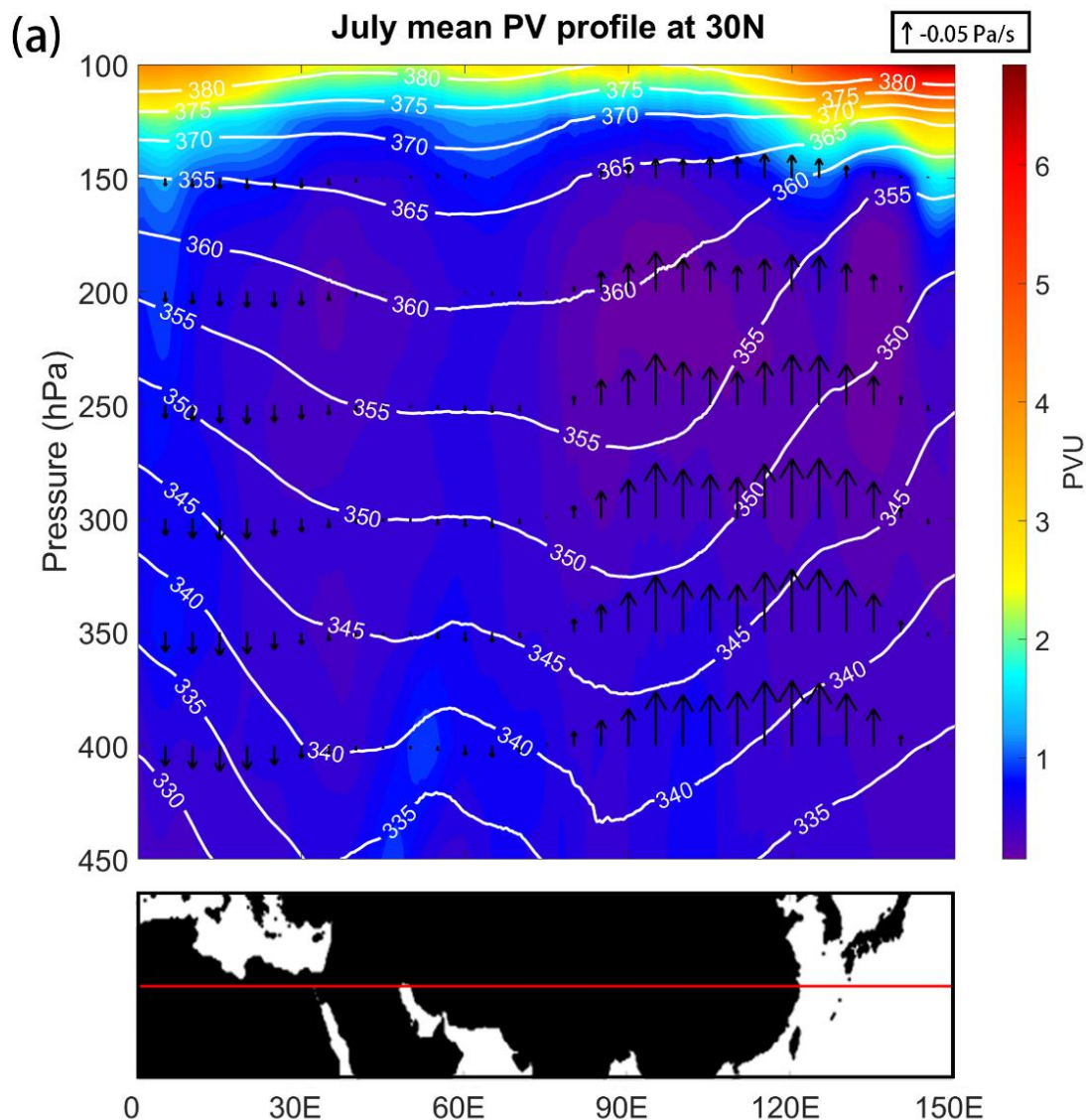


Figure 14. July mean zonal vertical profile at 30°N with isentropes (contour, in K), PV (shading, in PVU), and vertical velocity (arrow, in Pa/s) averaged from 1979 to 2020. (b) The schematic diagram of how the PV anomaly forms under PV perspective with isentropes (blue line), PV contour (red line), and horizontal wind direction (black symbols). (c) The schematic diagram of how apparent heating creates PV forcing.

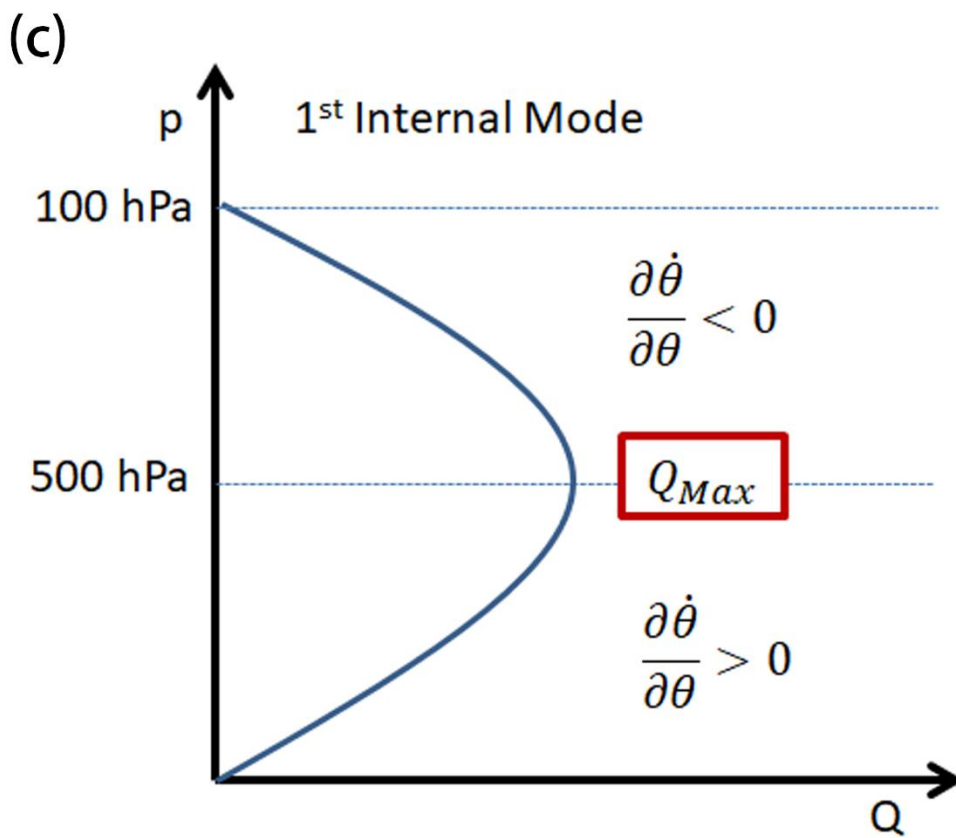
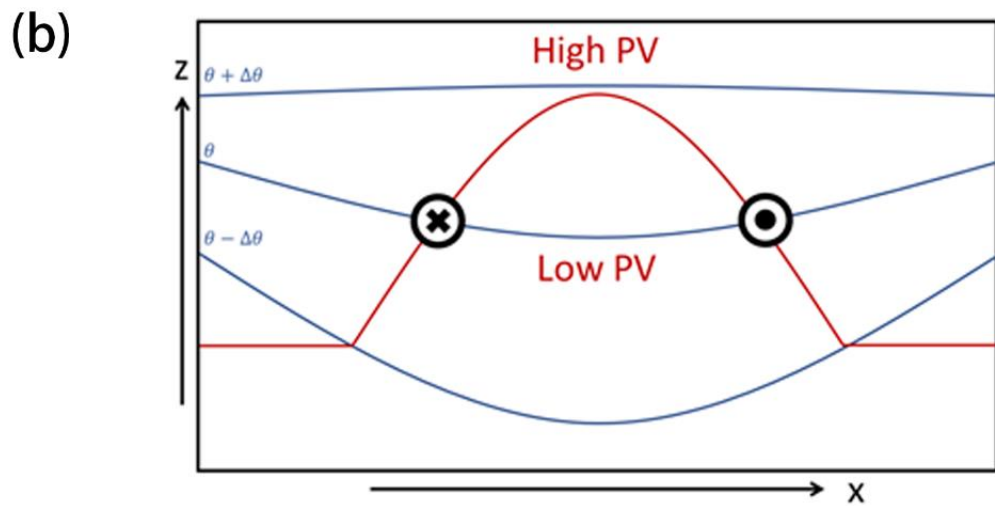


Figure 14. (continued)

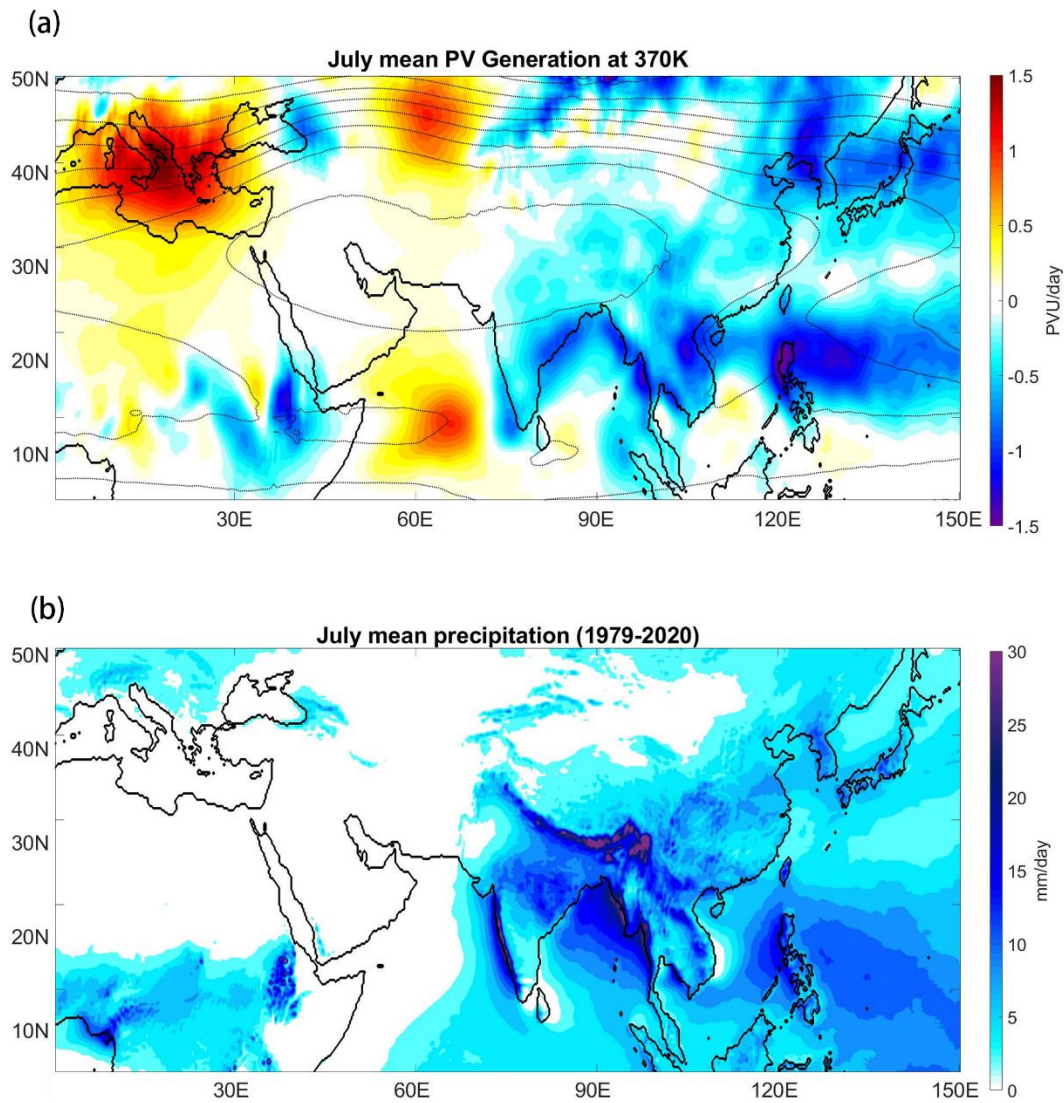


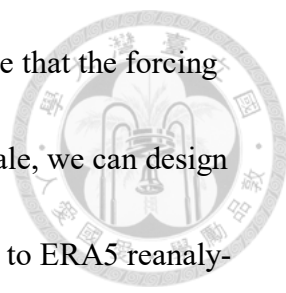
Figure 15. (a) July mean PV forcing (shading, in PVU/day) and PV (contour) at 370 K averaged from 1981 to 2020. (b) July monthly mean land precipitation (shading, in mm/day) averaged from 1981 to 2020.

4.4 The Vortex-Shedding Process and SAH



The annual variation of SAH is an important topic in dynamical climatology, including its change in strength and location. Fig. 16 shows the asymmetry of SAH on both monthly mean geopotential map and IPV map, but at different years. We can see the center of SAH is located either at east or west. Understanding the cause of asymmetry may be important for diagnose usage. The interesting part of this issue is that the asymmetry characteristic is not a stationary structure; instead, it is the mean state of weekly vortex-shedding process. Hsu and Plumb (2000) had built a shallow water model on β plane with the mean flow purely westward. With a consistent source of vorticity, they had found that the vortex would breakup into twice with the existence of non-linearity. They indicated that it is the eddy shedding process that causes the asymmetry structure of the SAH. However, the shape of SAH is not captured; nor did they discuss the story of the PV that is shed away.

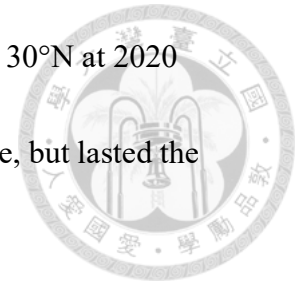
We would first revisit this vortex-shedding problem using the global SWQG model instead. It would be expensive to build a multilayer model calculating IPV. However, we may regard the mass between two isentropes as the shallow water system we want to solve. By placing a PV forcing above TP/ASM region with an idealized background flow, we can simulate the evolution of SAH PV in an idealized numerical experiment. When transforming IPV to shallow water PV (SWPV), we need



to be careful that the isentropic density should be multiplied. Assume that the forcing is steady and the background mean flow is persistent in a weekly scale, we can design an idealized numerical experiment. The parameters are approximate to ERA5 reanalysis data, including an elliptical constant PV forcing of maximum at $-6 \times 10^{-5} \text{ s}^{-1}/\text{day}$ (about -1.5 PVU/day for $\sigma = 40 \text{ kg m}^{-2} \text{ K}^{-1}$) with Gaussian shape, obtained from section 4.3, and an elliptical background vorticity produces the maximum wind speed at 30 m/s that does not evolve with time. We choose $\varepsilon = 300$ represented the first internal mode (cumulus heating) due to the heating structure obtained from fig. 13. Fig. 17 (a) shows the experiment design. Since realistic parameters are exerted and complete Coriolis force on the globe is applied, we would expect to get a more reasonable result.

Fig. 17 (b) shows the simulation result. We can see vortex-shedding from the heat source and finally become another center of the negative PV anomaly. The western center would be transported eastward by background mean flow, and absorbed by the eastern center, starting another cycle. This phenomenon can also be observed from the reanalysis data on IPV map, as shown in fig. 17 (c). Meanwhile, we can see the geopotential height on isobaric surface matches the PV distribution on isentropic surface in the mid-latitude, but cannot reflect PV near the equator. Namely, PV are presented in momentum field rather than in mass field in low-latitude, owing to the lack

of Coriolis force. The Hovmuller diagram of the geopotential along 30°N at 2020 summer (fig. 18) indicates that the oscillation is not a particular case, but lasted the whole summer.



We may discuss that is the non-linearity of the PV anomaly necessary for the eddy shedding process, or actually the pure advection process or linear Rossby wave propagation would cause the same result. Fig. 19 (a) compares the simulation result with the full dynamical process (with non-linear process, linear Rossby wave propagation and background mean flow) and with only pure advection process. The model result of pure advection does not contain the vortex-shedding process. Then we could indicate that the whole dynamics of eddy-shedding problem includes background advection and both linear and non-linear process, none of them are neglectable. Fig. 19 (b) the schematic diagram of the process. Unlike other synoptic scale systems, PV of SAH has notable non-linearity. That is to say, the relative vorticity has the same order comparing to the Coriolis parameter. It is a common misunderstanding and is worth highlighted.

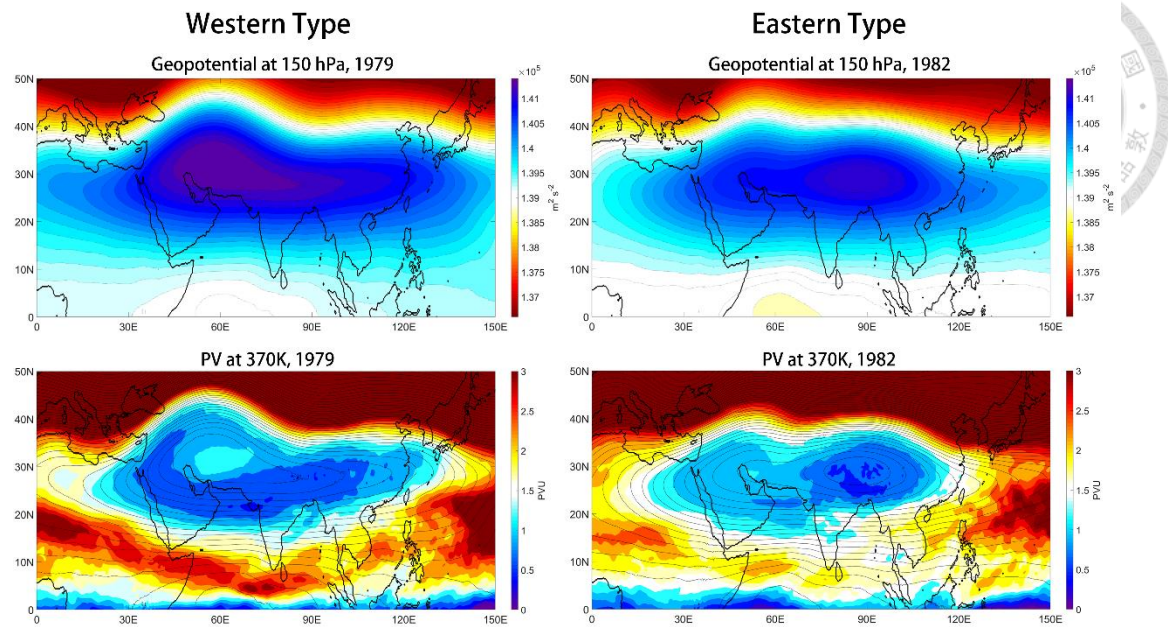


Figure 16. Top: July mean geopotential (shading, in m^2s^{-2}) on 150 hPa surface at 1979 (left), a western-type SAH and 1982 (right), an eastern-type SAH. Down: July mean PV (shading, in PVU) on 370K surface with geopotential on 150 hPa (contour, in m^2s^{-2}) at 1979(left), a western-type SAH and 1982 (right), an eastern-type SAH.

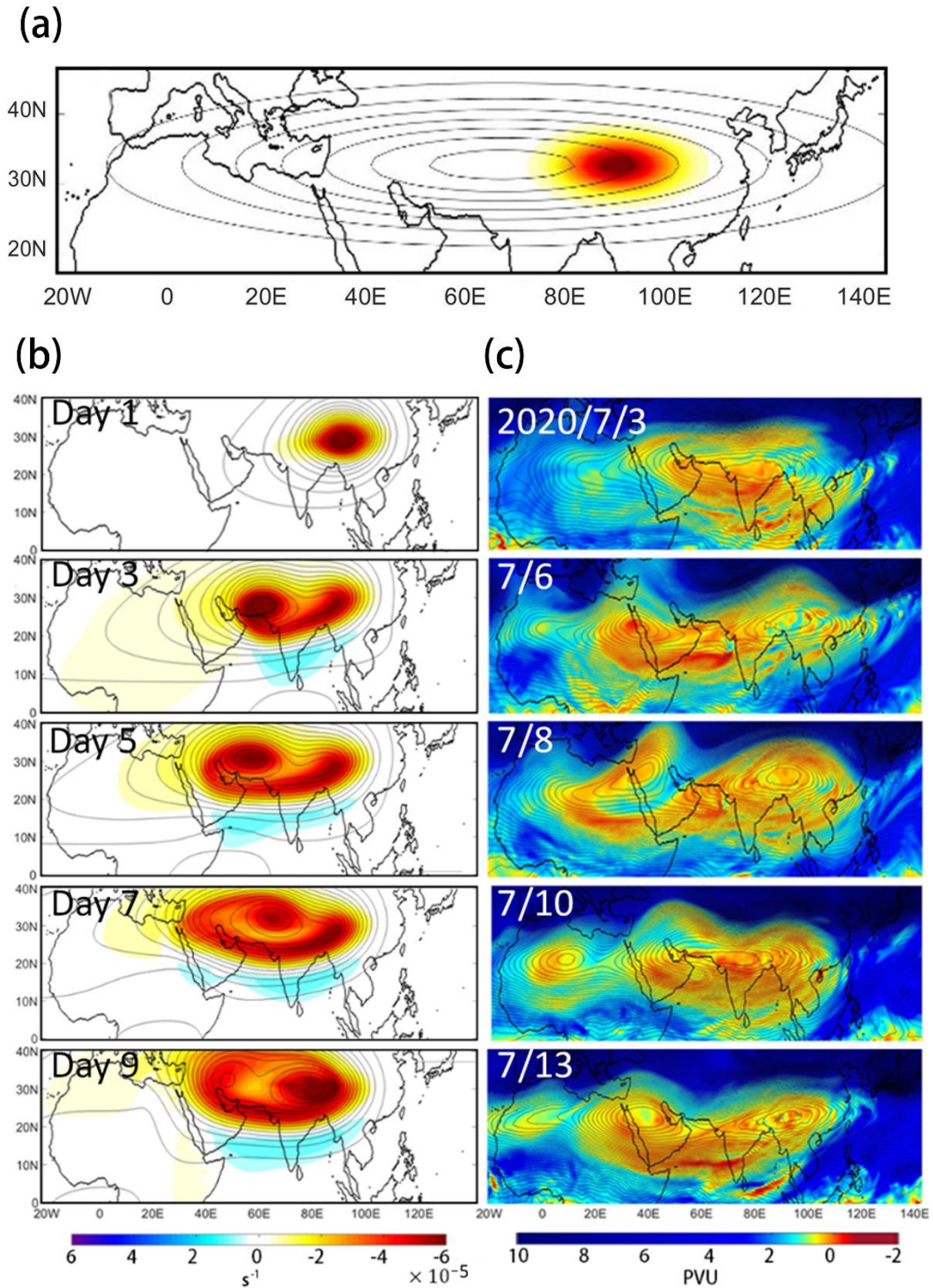


Figure 17. (a) The experiment design for SAH daily simulation with location of forcing (shading) and background vorticity (contour), which does not evolve with time. (b) SWQG model result time series with PV anomaly (shading, in s^{-1}) and height anomaly (contour). (c): reanalysis data with PV on 370 K (shading, in PVU), and geopotential on 150hPa (contour).

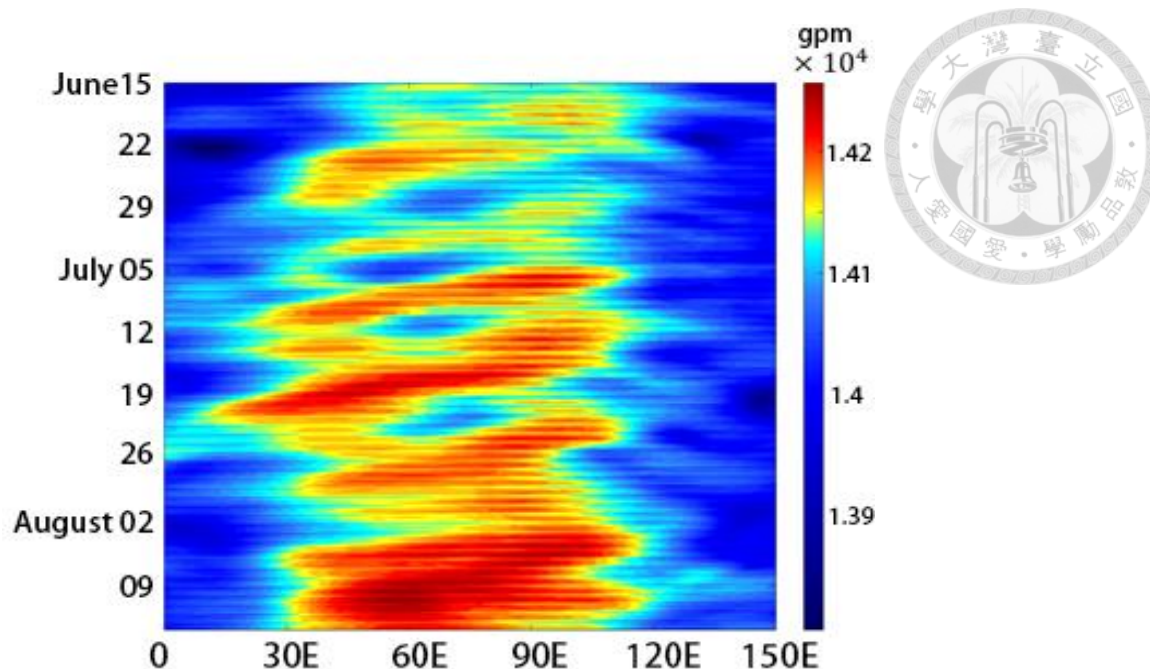


Figure 18. Hovmuller diagram of geopotential height (shading, in gpm) at 150 hPa surface along 30°N at 2020 summer.

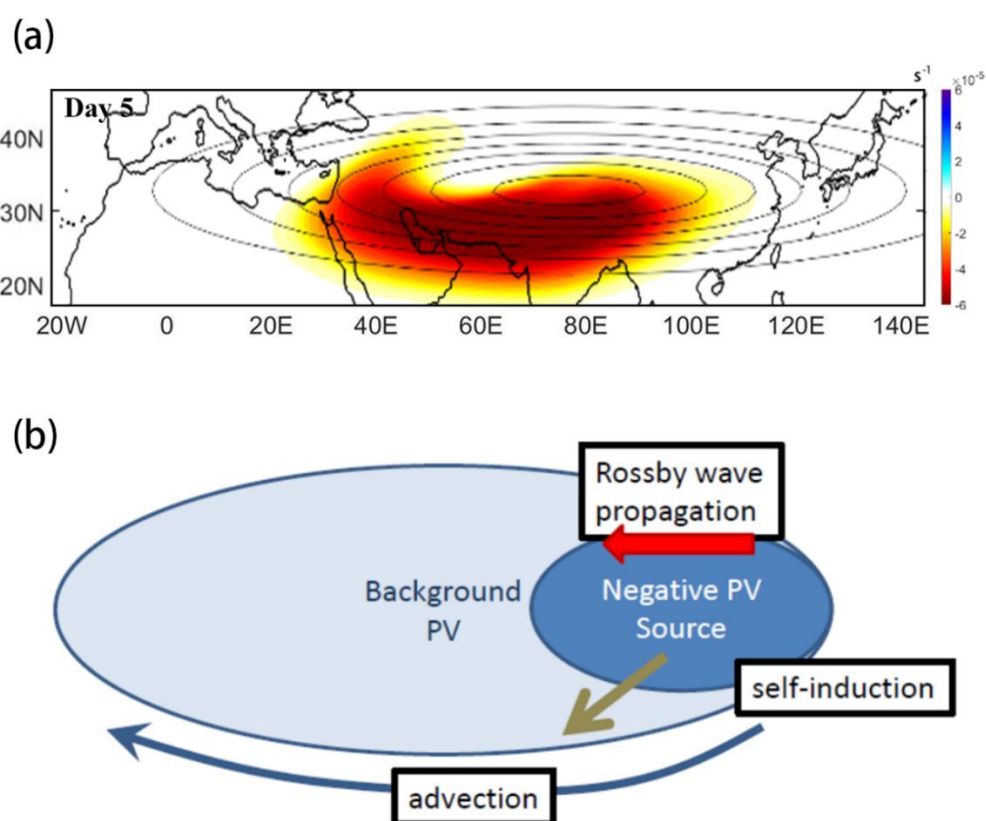
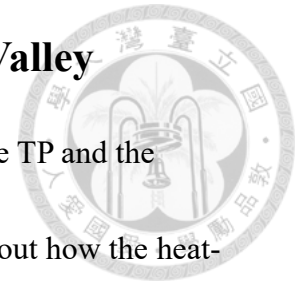


Figure 19. (a) SWQG model result with PV anomaly (shading, in s^{-1}) and background PV (contour) consider pure advection, integrated for 5 days. (b) Schematic diagram of the vortex-shedding dynamics.

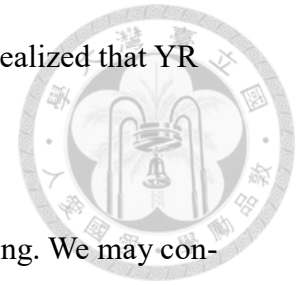
4.5 SAH and the Precipitation of Yangzi River Valley



Studies on the relationship between apparent heat source above TP and the strength of SAH is sufficient, and most of the papers are curious about how the heating above TP, or the intensity of SAH, influence heavy precipitation over YR valley during summer (Wu *et al* 2015; Ning *et al.* 2017; Ge *et al.* 2019). However, the mechanism of how apparent heat source from YR valley influence the strength and structure of SAH is still an undeveloped problem. In this research, we hypothesized the forcing from YR valley to be an important variable that affect the intensity and position of SAH. We have used statistical method and idealized numerical simulation to test the hypothesis.

Following the work of Ge *et al.* (2019), we build two indices of SAH for further analysis: SAH_INT index is defined as the sum of the geopotential height of all grid points in which the geopotential height is larger than 14,000 gpm, which delineates its intensity through its area; SAH_EW index is defined as the difference between the average geopotential height on the east (20°–35°N, 82.5°–115°E) and on the west (20°–35°N, 50°–82.5°E), which depicts the zonal varieties of SAH (Zhang and Qing, 2000). Correlating TP heating between $p_T=100$ hPa and $p_b=300$ hPa with SAH_INT index in July would produce a correlation coefficient $R = 0.46$, while the correlation between YR heating and SAH_INT index only gets $R = 0.18$. The result is just Ge *et*

al. 's (2019) statement and is not surprising since we have already realized that YR forcing only serves as the “perturbation” of the whole system.

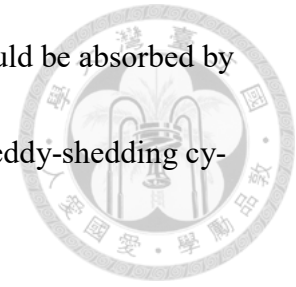


From the PV perspective, however, the topic becomes interesting. We may conduct the EOF analysis on IPV map over the area that has PV smaller than 1.5 PVU in the domain of $10^{\circ}-40^{\circ}\text{N}$, $0^{\circ}-120^{\circ}\text{E}$. Fig. 20 (a) shows the pattern of the first mode (EOF1, weighted 35.04%), while fig. 20 (b) the correlation between amplitude of EOF1 and YR monthly total precipitation. The correlation coefficient increases to $R = 0.38$.

There are two scientific questions to be answered from the statistical result: first, the pattern of the EOF1 shows that the variance of PV is more at the south-eastern side of that at the center of SAH. What is the mechanism behind the variant? The second question is, why we can see a stronger correlation between YR precipitation and the variance of PV, comparing that with the variance of geopotential? We may hypothesize that YR forcing, though being neglected in early research, actually serves as one of the main factors on SAH annual variability.

To verify the hypothesis, we may put a smaller but intense PV forcing ($-6 \times 10^{-5} \text{ s}^{-1}/\text{day}$) over YR region, and see how it evolves in the model (fig. 21 (a)). The magnitude of PV forcing is similar to the observation value we got from the section 4.3, covering the whole Tibet plateau and YR valley. We can observe that the

extra forcing over YR region would not be transported alone; it would be absorbed by the main vortex, causing the enhancement of PV (fig. 21 (b)). The eddy-shedding cycle would also be postponed.



We may do a further examination by finding the difference with and without YR forcing. Using the 5-7 days averaged integration result, the PV difference is shown in fig. 22. It has a really similar pattern comparing to the EOF1. Moreover, we may do the sensitivity test to check that is it the intensity of the perturbation PV forcing above YR that changes the speed of vortex-shedding process, or simply the intensity of PV forcing would postpone the translation speed. By changing the PV forcing of YR region, results show that the intensity of the main vortex does not affect the translation speed, but the intensity of YR forcing would slow down the vortex-shedding cycle (fig. 23).

From the discussion of the model outputs, we may surmise that there exist relationships between YR precipitation and SAH location. Disappointedly, the correlation between SAH_EW and YR precipitation is merely at $R = 0.06$. Yet, by observing the SAH_EW index with strong precipitation years (1981, 1983, 1991, 1993, 1996, 1998, 2020), we find that none of those years has SAH center located at the west. In conclusion, severe precipitation might impede the vortex-shedding process and shifts the center of SAH to the east, and further analysis with complex model simulation should

be done on this topic.

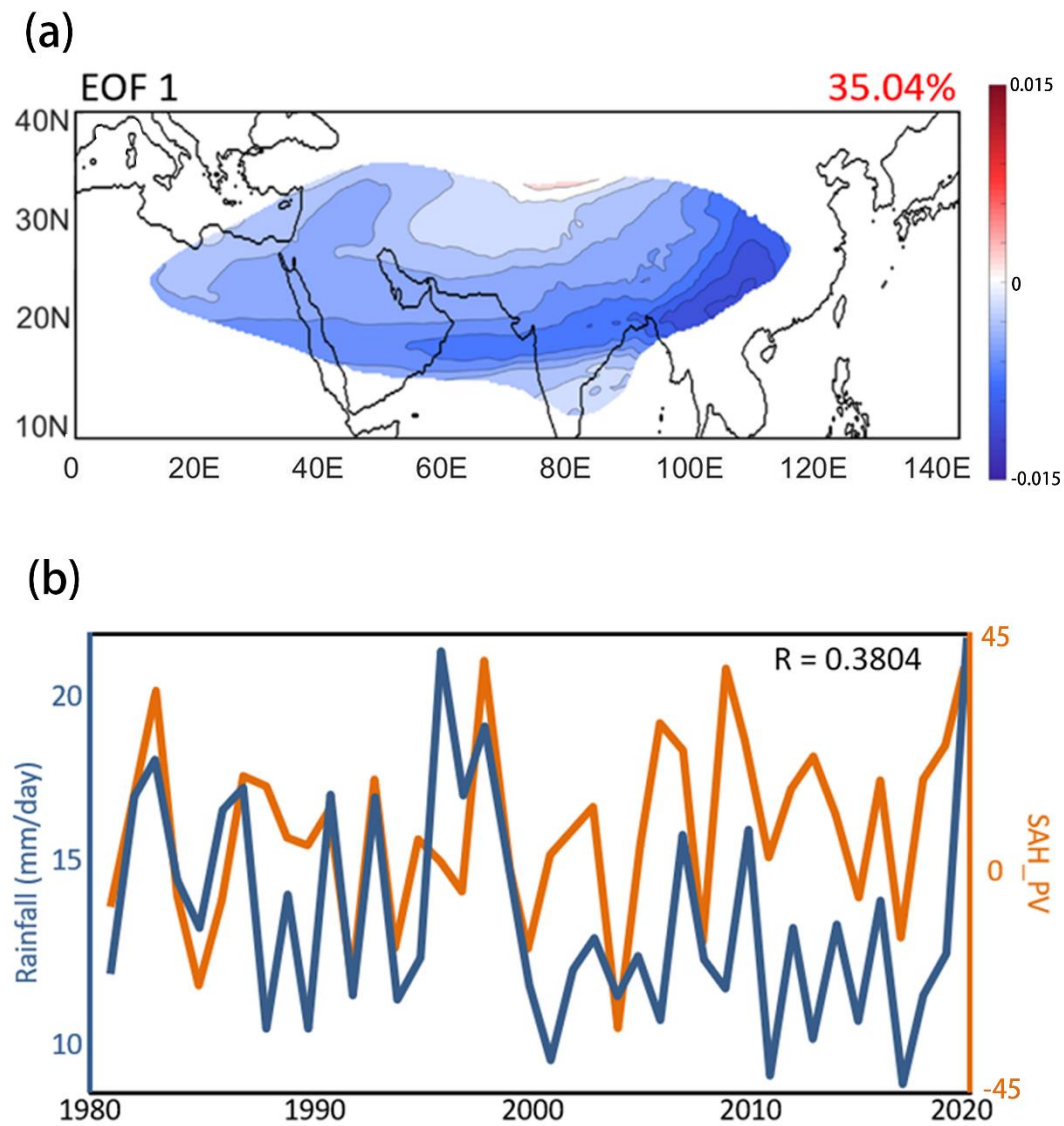
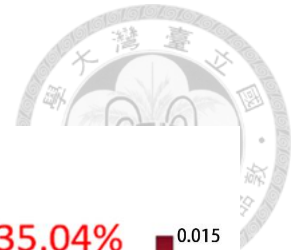


Figure 20. (a) The pattern of first mode of SAH PV in July under EOF analysis (shading). (b) Correlation between Julys mean precipitation over YR (blue) and amplitude of the first mode (orange).

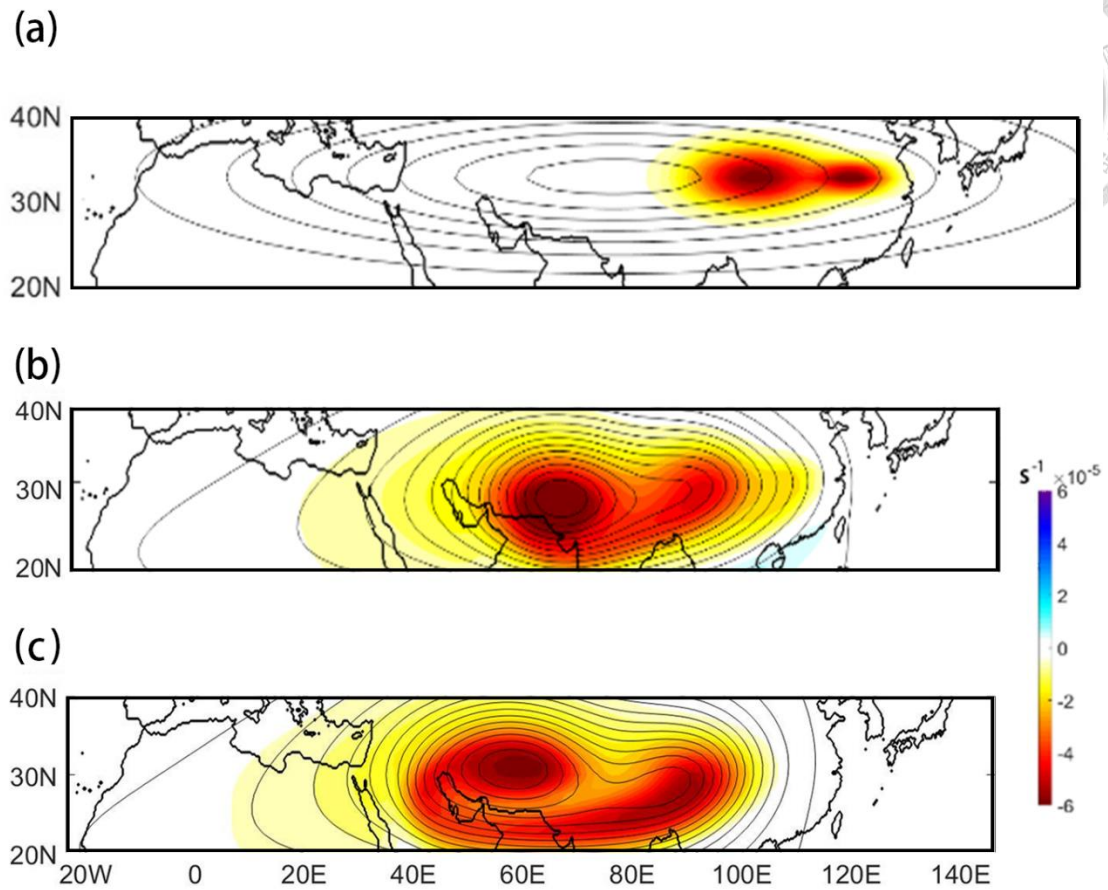


Figure 21. (a) Same as fig. 17 (a), but adding an extra forcing above YR valley. (b) SWQG model result with PV anomaly (shading, in s^{-1}) and height anomaly (contour) adding YR forcing, integrated for 5 days. (c) same as (b), but without YR forcing.

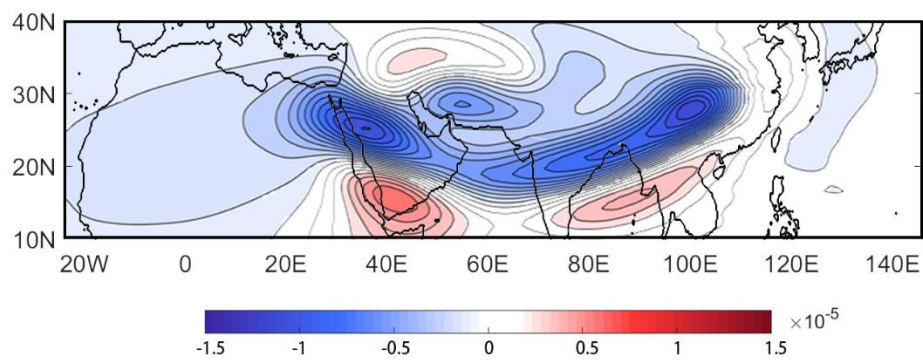


Figure 22. The 5-7 days averaged PV difference (shading, in s^{-1}) between the pure TP forcing experiment and YR forcing added experiment. The YR forcing would enhance the PV intensity of SAH.

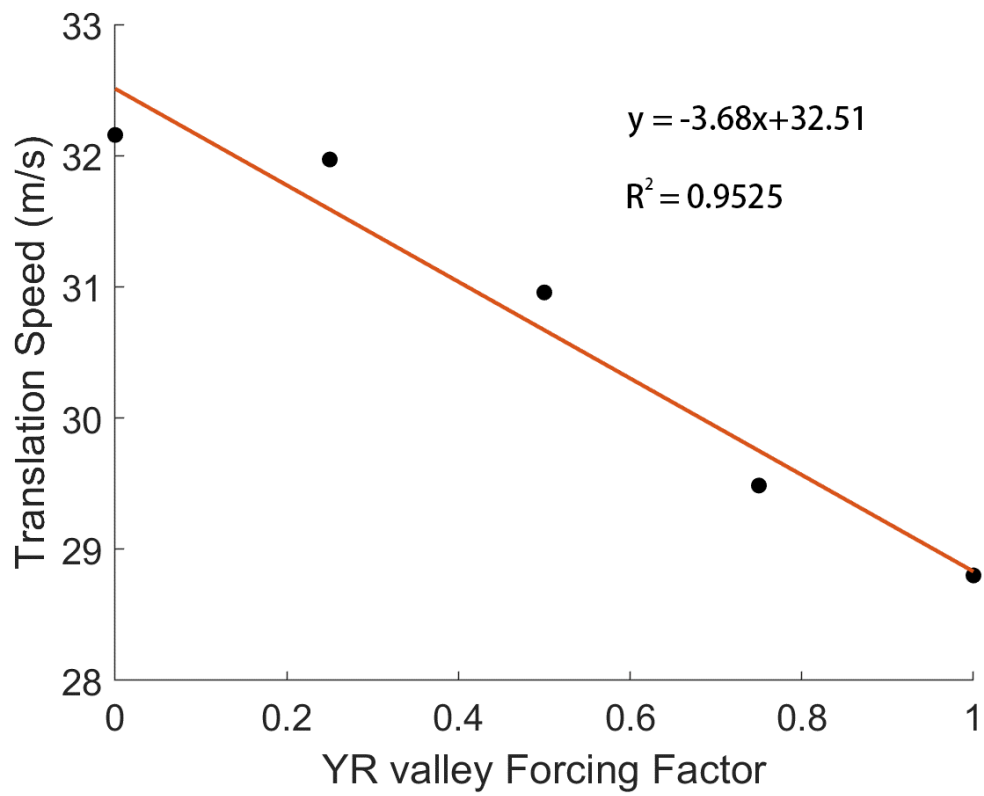


Figure 23. The sensitivity test of the YR valley forcing with the translation speed. The amplitude of YR forcing is set to be $-6 \times 10^{-5} \text{ s}^{-1}/\text{day} \times \text{Forcing Factor}$.

4.6 SAH and the Vertical Motion above Eurasian



As mentioned in section 4.4 and in fig. 16, the July mean geopotential height map shows different types of SAH: the western type (10 out of 42 years) and the eastern type of SAH (12 out of 42 years), with others to be double centered (20 out of 42 years). The vertical motion and geopotential height on 150 hPa surface are shown in fig. 24. It is engrossing that vertical motion is well coupled with the SAH center: upward motion locates at the east of SAH center, while downward motion at the west. The western type of SAH would cause a smaller range, but more intense subsidence at the Mediterranean, while the eastern type causes a wide range of subsidence. This exploration may be explained by Sverdrup balance theory, by reason of the small horizontal advection term in SAH. The equation can be written as:

$$\beta v_g = f \frac{\partial \omega}{\partial z}. \quad (4.5)$$

At the east side of an anti-cyclonic circulation, there would be divergence at the upper troposphere and causes upward motion, while it would be convergence and downward motion at the west side. We may also hypothesize that the intensification of SAH may enhance the upward motion on the east and increase the rainfall. Moreover, combining the arguments in section 4.5, a positive feedback might occur due to the strengthening and east-shifting of SAH. Also, the traditional “monsoon-desert coupling” mechanism had pointed out that the more the precipitation at ASM may

cause stronger subsidence motion above the Mediterranean. However, if the precipitation at EASM would change the shape of SAH, causing the center of SAH to move east, the subsidence above the Mediterranean may actually be weaker. This thesis simply points out this phenomena and would not perform a detailed analysis on this topic; however, it is an interesting topic that worth discussing.

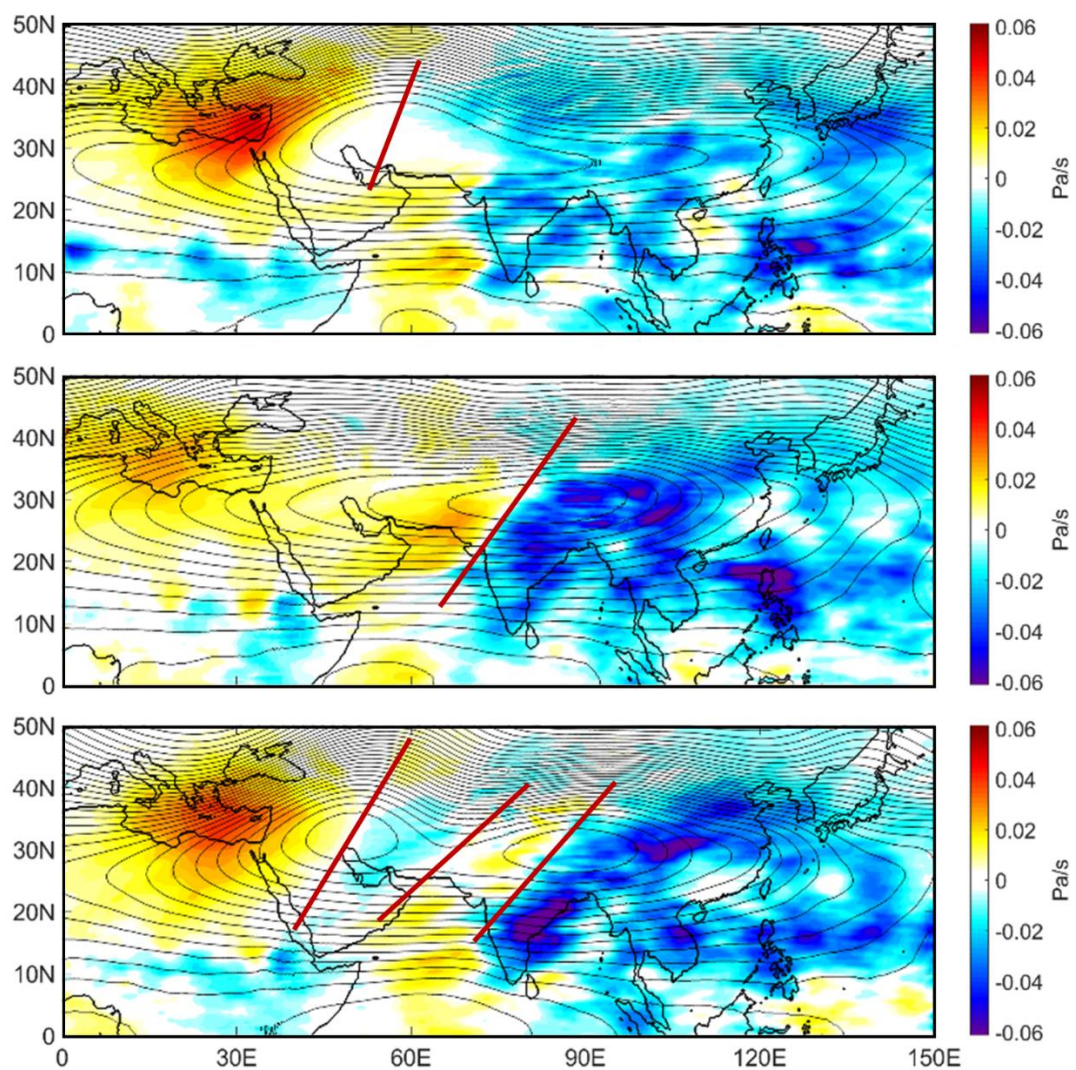


Figure 24. ω (shading, in Pa/s) and geopotential height (contour) patterns at (a) western type (b) eastern type (c) double centered of SAH.

CHAPTER 5

Conclusion



In this study, we have established a PV perspective analysis on SAH thoroughly.

An idealized global SWQG model is built as our tool for numerical experiments. Vortex-shedding experiment is conducted, and we can observe the eddy-shedding cycle through the numerical experiments. The simulation result captures the PV pattern of ERA5 reanalysis data on 370 K IPV map well, and we can explain the asymmetry of monthly mean SAH through this process.

Early research had found positive correlations between SAH intensity (defined by its geopotential) and YR valley precipitation statistically, but without physical explanation. Thus, we tried to explain these phenomena through a dynamical view.

Through the EOF analysis of SAH PV, we discover that the pattern of EOF1 is similar to the PV transporting path and shows high positive correlation with the YR precipitation. Our statement stands that the PV forcing from YR latent heat release serves as an important factor enhancing the intensity of SAH, leaving impacts on the annual variations that cannot be ignored.

This phenomenon is hard to be observed from geopotential map, and we should claim that PV analysis has a lot advantage comparing to the geopotential height analysis on SAH. The reason is that PV generated from YR valley is the slave comparing to

the large and persistent forcing on TP, and PV would mixed into the main structure.

When PV anomaly is propagated to the lower latitude region, we could not observe the signal on geopotential height map due to the lack of the Coriolis force and the mass response. The signal would again to appear when the PV anomaly is propagated to the northwest. Numerical experiments had confirmed this argument, and we also state that the global SWQG model might be a useful tool when diagnosing the subtropics, as it serves as the transition zone between the mid-latitude with strong Coriolis effect and the tropics with no Coriolis force.

Meanwhile, the PV forcing on YR may postpone the speed of vortex-shedding, thus we have hypothesized that heavy precipitation may corresponds to the east-shifting of the SAH. The low correlation indicates that there may be more complex physics behind. However, we observed that severe rainfall events only occur if the center of SAH is not at west. Still, we would highlight again that PV perspective on SAH, though stagnates in recent years, is still a powerful insight and reveals the hidden secrets of the dynamics behind this enormous system.

At the end, we discuss how the pattern of SAH affects the vertical motion. We realize that SAH is actually under Sverdrup balance. We have pointed out that the shape of SAH would affect the strength of subsidence over the Mediterranean, and the

precipitation over YR valley may influence the shape of SAH. The traditional monsoon-desert mechanism of “wet gets wetter, dry gets drier” may be revised by this new discovery.



Reference



Arfken, G.B., and H. J. Weber, 2001: Mathematical methods for physicists (5th Ed.) Harcourt

Academic Press, 1112 pp.

Charney, J. G., M. E. Stern, 1962: On the Stability of Internal Baroclinic Jets in a Rotating Atmosphere. *J. Atmos. Sci.* 19 (2): 159–172.

Duan, A. M., and G. Wu, 2005: Role of the Tibetan Plateau thermal forcing in the summer climate patterns over subtropical Asia. *Clim. Dyn.* 24, 793–807.

Ertel, H., 1942: Ein neuer hydrodynamische wirbelsatz. *Meteor.Z. Braun-schweig.*, 59, 33–49.

Fulton, S. R., and W. H. Schubert, 1985: Vertical normal mode transforms: Theory and application. *Mon. Wea. Rev.*, 113, 647–658.

Ge, J., Q. You, Y. Zhang, 2019. Effect of Tibetan Plateau heating on summer extreme precipitation in eastern China. *Atmos. Res.* 218, 364–371.

Haynes, P. H., and M. E. McIntyre, 1987: On the evolution of vorticity and potential vorticity in the presence of diabatic heating and friction or other forces. *Journal of Atmospheric Sciences*, 44:828–841.

He, H. J., W. McGinnis, Z. Song, M. Yanai, 1987: Onset of the Asian summer monsoon in 1979 and the effect of the Tibetan Plateau. *Mon. Wea. Rev.* 115:1966–1995.

Hoskins, B. J., 2015: Potential vorticity and the PV perspective. *Adv. Atmos. Sci.*, 32, 2–9.

Hoskins, B. J., M. McIntyre, and A. Robertson, 1985: On the use and significance of isentropic potential vorticity maps. *Quart. J. Roy. Meteor. Soc.*, 111, 877–946.

Hsu, C. J., and R. A. Plumb, 2000: Nonaxisymmetric thermally driven circulations and upper-tropospheric monsoon dynamics, *J. Atmos. Sci.*, 57, 1255–1276.

Liu, Y. M., G. X. Wu, H. Liu, P. Liu, 2001: Condensation heating of the Asian summer monsoon and the subtropical anticyclone in the Eastern Hemisphere. *Clim. Dyn.* 17:327–338.

Lorenz, E. N., 2006: Reflections on the Conception, Birth, and Childhood of Numerical Weather Prediction, *Annu. Rev. Earth Planet. Sci.*, Vol. 34, 37–45.

Matsuno, T., 1966: Quasi-Geostrophic Motions in the Equatorial Area, *J. Meteorol. Soc. Jpn.*, 44, 25–43.

Ning, L., J. Liu, and B. Wang, 2017: How does the South Asian High influence extreme precipitation over eastern China? *J. Geophys. Res. Atmos.* 122, 4281–4298.

Rodwell, M. J., B. J. Hoskins, 1996: Monsoon and the dynamics of deserts. *Q. J. R. Meteorol. Soc.* 122:1385–1404.

——, ——, 2001: Subtropical anticyclones and summer monsoons. *J. Clim.* 14:3192–3211.



Rossby, C. G., Collaborators, 1939: Relation between variations in the intensity of the zonal circulation of the atmosphere and the displacements of the semi-permanent centers of action. *Journal of Marine Research*. 2 (1): 38–55.

Schubert, W. H., R. K. Taft, L. G. Silvers, 2009: Shallow water quasi-geostrophic theory on the sphere. *J. Adv. Model. Earth Syst.*, 1(2), doi:10.3894/JAMES.2009.1.2.

Verkley, W. T. M., 2009: A balanced approximation of the one layer shallow-water equations on a sphere. *J. Atmos. Sci.*, 66, 1735–1748.

Wu, G., A. Duan, Y. Liu et al., 2015: Tibetan Plateau climate dynamics: recent research progress and outlook. *National Science Review*, 2, 100–116.

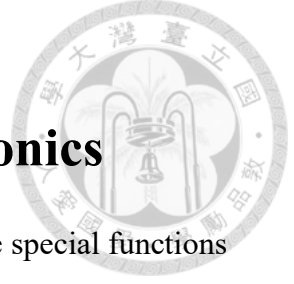
Yanai, M., S. Esbensen, J. H. Chu, 1973: Determination of bulk properties of tropical cloud clusters from large-scale heat and moisture budgets. *J. Atmos. Sci.* 30, 611–627.

Yanai, M., and C. Li, 1994: Mechanism of heating and the boundary layer over the Tibetan Plateau. *Mon. Wea. Rev.* 122:305–323.

Zhang, Q., and Y. Qian, 2000: Interannual and Interdecadal variations of the South Asia High (in Chinese), *Chin. J. Atmos. Sci.*, 24, 67–77.

APPENDIX A

Spherical and Spheroidal Harmonics



Spherical harmonics (Y_{mn}) and spheroidal harmonics (S_{mn}) are special functions defined on the surface of a sphere, and both of them form a complete set of orthogonal functions. Spherical harmonics are the solution of the Laplace's equation in spherical coordinates (also called the spherical harmonic differential equation), and can be written as (Arfken, 2001)

$$Y_{mn}(\lambda, \phi) = (-1)^m \sqrt{\frac{(2n+1)(n-m)!}{4\pi(n+m)!}} P_n^m \cos \phi e^{im\lambda}, \quad (\text{A.1})$$

with n the total wave number, m the zonal wave number, λ the longitude, ϕ the latitude, and P_{mn} the associated Legendre polynomials

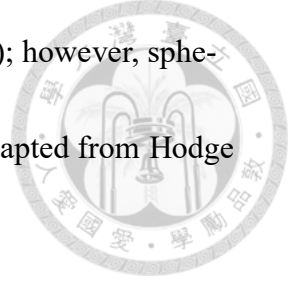
$$P_n^m(\mu) = (1-\mu)^{m/2} \frac{d^m}{d\mu^m} P_n^m(\mu). \quad (\text{A.2})$$

The associated Legendre polynomials are the solution of the associated Legendre equation

$$(1-\mu^2) \frac{\partial}{\partial \mu^2} P_n^m(\mu) - 2\mu \frac{\partial P_n^m(\mu)}{\partial \mu} + \left[n(n+1) - \frac{m^2}{1-\mu^2} \right] P_n^m(\mu) = 0, \quad (\text{A.3})$$

while the spheroidal harmonics are the solution of spheroidal wave equation (2.31). A more detailed introduction and proof on the properties of spherical harmonics can be found in Arfken (1985).

Spherical harmonics can be obtained analytically through (A.2); however, spheroidal harmonics can only be computed numerically. The method adapted from Hodge (1970) are as follows.



Consider the associated Legendre expansion

$$S_{mn}(\epsilon; \mu) = \sum_{r=0,1}^{\infty} d_r^{mn}(\epsilon) P_{m+r}^m(\mu), \quad (\text{A.4})$$

where $r = 1$ if $n - |m|$ is even and $r = 0$ if $n - |m|$ is odd. $d_r^{mn}(\epsilon)$ is called the expansion coefficients of $S_{mn}(\epsilon; \mu)$ to the associated Legendre polynomial $P_{m+r}^m(\mu)$, which satisfied the differential equation (A.3), and the orthonormality condition

$$\frac{1}{2} \int_{-1}^1 P_n^m(\mu) P_{n'}^m(\mu) d\mu = \begin{cases} \frac{1}{(2n+1)} \frac{(n+m)!}{(n-m)!} & n' = n \\ 0 & n' \neq n. \end{cases} \quad (\text{A.5})$$

Substitute (A.2) into the spheroidal wave equation (2.31), then using (A.3), we obtain

$$\sum_{r=0,1}^{\infty} d_r^{mn}(\epsilon) [\alpha_{mn}(\epsilon) - (m+r)(m+r+1) - \epsilon\mu^2] P_{m+r}^m(\mu) = 0. \quad (\text{A.6})$$

With the recurrence relation of associated Legendre polynomials

$$\mu P_n^m(\mu) = \frac{(n+m)P_{n-1}^m(\mu) + (n-m+1)P_{n+1}^m(\mu)}{(2n+1)}, \quad (\text{A.7})$$

we may derive that

$$\begin{aligned} \mu^2 P_n^m(\mu) &= \frac{(n-m+1)(n-m+2)}{(2n+1)(2n+3)} P_{n+2}^m(\mu) \\ &\quad + \frac{2n(n+1) - 2m^2 - 1}{(2n-1)(2n+3)} P_n^m(\mu) \\ &\quad + \frac{(n+m-1)(n+m)}{(2n-1)(2n+1)} P_{n-2}^m(\mu) \end{aligned} \quad (\text{A.8})$$

Substitute (A.8) into (A.6), we would obtain the recurrence relation of the expansion coefficients

$$A_r^m(\epsilon)d_{r+2}^{mn}(\epsilon) + [B_r^m(\epsilon) - \alpha_{mn}(\epsilon)]d_r^{mn}(\epsilon) + C_r^m(\epsilon)d_{r-2}^{mn}(\epsilon) = 0, \quad (\text{A.9})$$

Where

$$\begin{aligned} A_r^m(\epsilon) &= \left(\frac{(2m+r+2)(2m+r+1)}{(2m+r+3)(2m+r+5)} \right) \epsilon, \\ B_r^m(\epsilon) &= (m+r)(m+r+1) + \left(\frac{2(m+r)(m+r+1) - 2m^2 - 1}{(2m+2r-1)(2m+2r+3)} \right) \epsilon, \\ C_r^m(\epsilon) &= \left(\frac{r(r-1)}{(2m+2r-3)(2m+2r+1)} \right) \epsilon. \end{aligned} \quad (\text{A.10})$$

We may convert the problem (A.9) into a simple tridiagonal form by re-indexing

$$\begin{aligned} D_q &= C_{2q+s}^m(\epsilon), & E_q &= B_{2q+s}^m(\epsilon), \\ F_q &= A_{2q+s}^m(\epsilon), & a_q &= d_{2q+s}^{mn}(\epsilon), \end{aligned} \quad (\text{A.11})$$

where $s = 0$ if $n-|m|$ is even and $s = 1$ if $n-|m|$ is odd. (A.9) can be rewritten as

$$D_q a_{q-1} + [E_q - \alpha] a_q + F_q a_{q+1} = 0, \quad \text{for } q \geq 0. \quad (\text{A.12})$$

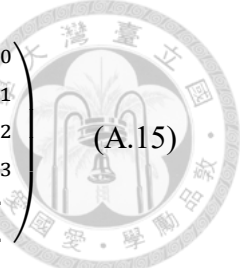
Now we need to convert (A.12) to a tridiagonal, symmetric matrix problem. Define

$$a_q = \left(\frac{D_1 D_2 D_3 \dots D_q}{F_0 F_1 F_2 \dots F_{q-1}} \right) b_q \quad (\text{A.13})$$

and substitute into (A.12) yields

$$(D_q F_{q-1})^{1/2} b_{q-1} + [E_q - \alpha] b_q + (D_{q+1} F_q)^{1/2} b_{q+1} = 0, \quad \text{for } q \geq 0, \quad (\text{A.14})$$

or in the matrix form



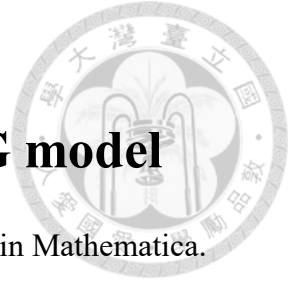
$$\begin{pmatrix} E_0 & (D_1 F_0)^{1/2} & 0 & 0 & \dots \\ (D_1 F_0)^{1/2} & E_1 & (D_2 F_1)^{1/2} & 0 & \dots \\ 0 & (D_2 F_1)^{1/2} & E_2 & (D_3 F_2)^{1/2} & \dots \\ 0 & 0 & (D_3 F_2)^{1/2} & E_3 & \dots \\ \vdots & \vdots & \vdots & \vdots & \ddots \end{pmatrix} \begin{pmatrix} b_0 \\ b_1 \\ b_2 \\ b_3 \\ \vdots \end{pmatrix} = \alpha \begin{pmatrix} b_0 \\ b_1 \\ b_2 \\ b_3 \\ \vdots \end{pmatrix} \quad (\text{A.15})$$

The eigenvalues $\alpha_{mn}(\epsilon)$ and eigenfunctions $S_{mn}(\epsilon, \mu)$ are computed as follows.

We should first compute D_q, E_q and F_q from (A.11) with $s = 0$ and $s = 1$ for particular wavenumbers m respectively. Plug the result into tridiagonal eigensystem problem (A.15), then convert b_q to a_q through (A.13), and a_q to d_{2q+s}^{mn} via (A.11). Having the expansion coefficients allows us to calculate the eigenvalues and eigenfunctions. Remember to normalize the eigenfunctions so that they would satisfy (3.1). In appendix B we would show how to calculate the eigenvalue using this method.

APPENDIX B

Programming of the Global SWQG model



The program for obtaining the spheroidal harmonics is written in Mathematica.

The code is listed below:

```
SetDirectory[NotebookDirectory[]];
S[ε_, n_, m_, μ_, φ_] := N[SpheroidalPS[n, m, √ε, μ], 20];
generateAllFiles[ε_, Nmax_, mashTheta_] := Block[
  {n, m, μ, φ, res1, res2, Name1, Name2, e1, e2},
  For[n = 0, n <= Nmax, n++,
    For[m = -n, m <= n, m++,
      res1 =
        Table[μ = -1 + (2 i - 1)/ mashTheta ;
          S[ε, n, m, μ, φ], {i, 1, mashTheta}] //
        Name1 =
          "e" <> ToString[ε, InputForm] <> "n" <>
            ToString[n, InputForm] <> "m" <> ToString[m, InputForm] <>
              ".txt";
          e1 = Export[Name1, Part[res1, 2], "Table"];
        ];
      ];
  ];
ε = ____; mashTheta = ____; mashPhi = ____; Nmax = ____;
generateAllFiles[ε, Nmax, mashTheta]
```

mashTheta is for the spatial resolution, while Nmax the cutoff wavenumber. Change

SpheroidalPS to SpheroidalPSPrime would get the derivatives of the harmonics.

The main program for calculating dq/dt is written as a function in matlab. Here we would list the spectrum-transforming codes of the program. P and dP are the $S_{mn}(\epsilon; \mu)$ and $DS_{mn}(\epsilon; \mu)$ in the thesis content, Alpha is the eigenvalue, while n_grid the spatial resolution and the n_max cutoff wavenumber. Here we would introduce the important variables we used.

n_grid : the resolution is $(n_grid+1, 2* n_grid)$. Set to be 120 in this thesis.

n_max : the cutoff wavenumber. Set to be 80 in this thesis.

P : the 1D basis, or called the associated Legendre polynomial if talking about spherical harmonics. It is a 3D array with size $(n_grid+1, n_max+1, 2* n_max+1)$.

dP : same as P , but the 1st order derivative on meridional direction of the basis.

Alpha : the eigenvalue, which is a 2D array with size $(n_max+1, 2* n_max+1)$.

q : initial value of PV anomaly, which is a 2D array with size $(n_grid+1, 2* n_grid)$.

The sorting of the basis is easy. $S_{mn}(\epsilon; \mu)$ is at the location of $P(:, n+1, m+ n_max+1)$, while α_{mn} is located at $\text{Alpha}(n+1, -m+1)$ if $m < 0$ and $\text{Alpha}(n+1, m+1)$ if $m > 0$. We would first show how to calculate the eigenvalue using the method in appendix A.

```

function[Alpha] = find_alpha(n_max,epsilon)
r_max = n_max+2;
m_max = n_max+2;
for m = 0:m_max
    %% Calculate ABC
    for R = 0:r_max
        A(R+1) = (2*m+R+2)*(2*m+R+1)/((2*m+2*R+3)*(2*m+2*R+5))*epsilon;
        B(R+1) = (m+R)*(m+R+1)+((2*(m+R)*(m+R+1)-2*m^2-1)/((2*m+2*R-1)*(2*m+2*R+3)))*epsilon;
        C(R+1) = (R*(R-1)/((2*m+2*R-3)*(2*m+2*R-1)))*epsilon;
    end
    %% Calculate DEF
    for r = 0:r_max
        q = floor(r/2);
        if mod(r,2) == 0    % Even
            D_even(q + 1) = C(2*q + 1);
            E_even(q + 1) = B(2*q + 1);
            F_even(q + 1) = A(2*q + 1);
        else                % Odd
            D_odd(q + 1) = C(2*q + 2);
            E_odd(q + 1) = B(2*q + 2);
            F_odd(q + 1) = A(2*q + 2);
        end
    end
    %% Reconstruct the Matrix
    for i = 1:floor(r_max/2)
        for j = 1:floor(r_max/2)
            if i == j
                Matrix_even(i,j) = E_even(j);
            end
            if i-j == 1
                Matrix_even(i,j) = (D_even(i)*F_even(j))^(1/2);
            end
            if j - i == 1
                Matrix_even(i,j) = (D_even(j)*F_even(i))^(1/2);
            end
        end
    end
end

```


```

%% Trans b to a
[b_odd,Alpha_odd] = eig(Matrix_odd);
[b_even,Alpha_even] = eig(Matrix_even);
D_cumprod = 1; F_cumprod = 1; L = length(D_even);
for i = 1:L-1
    D_cumprod = D_cumprod*D_even(i+1);
    F_cumprod = F_cumprod*F_even(i);
end
a_even = sqrt(D_cumprod/F_cumprod)*b_even;
D_cumprod = 1; F_cumprod = 1; L = length(D_odd);
for i = 1:L-1
    D_cumprod = D_cumprod*D_odd(i+1);
    F_cumprod = F_cumprod*F_odd(i);
end
a_odd = sqrt(D_cumprod/F_cumprod)*b_odd;

%% This part is for beautiful listing
Alpha_odd = diag(Alpha_odd);
Alpha_even = diag(Alpha_even);
for i = 1:length(Alpha_even)
    Alpha(2*i - 1) = Alpha_even(i);
    Alpha(2*i) = Alpha_odd(i);
end
Alpha_list(m+1,:) = Alpha;
end
L = length(Alpha_list)-2;
for i = 0:L
    for j = 0:L
        if j>=i
            new_Alpha_list(j+1,i+1,:) = Alpha_list(i+1,j-i+1,:);
        end
    end
end
Alpha = new_Alpha_list;

```

Here is the codes for finding the dq/dt .



```
function[dqdt] = find_dqdt(q,P,dP,Alpha,n_grid,n_max)
(…) % Environmental settings
for n = 0:n_max
    for m = -n:n
        % Change the 1-dim basis to Harmonics
        for ind = 1:n_grid*2
            S(:,ind) = P(:,n+1,m+n_max+1)*exp(li*m*lambda(ind));
            dS(:,ind) = dP(:,n+1,m+n_max+1)*exp(li*m*lambda(ind));
        end
        S_conj = conj(S);
        % Obtain q_mn and psi_mn
        q_mn = sum(sum(q.*S_conj))*dmu*dlambda/(4*pi);
        if m < 0
            nu = 2*Omega*m/Alpha(n+1,-m+1);
            psi_mn = -a^2*q_mn/Alpha(n+1,-m+1);
        else
            nu = 2*Omega*m/Alpha(n+1,m+1);
            psi_mn = -a^2*q_mn/Alpha(n+1,m+1);
        end
        % Find differentiation in physical space
        % find_dlambda is a function finding zonal differentiation using FFT
        psi = psi + real(S*psi_mn);
        dqdmu = dqdmu + real(dS*q_mn);
        dpdmu = dpdmu + real(dS*psi_mn);
    end
end
dqdl = find_dlambda(q,n_grid); dpdl = find_dlambda(psi,n_grid);
Ros = Ros + real(S*q_mn*li*nu); % The linear part
J = (dpdl.*dqdmu - dqdl.*dpdmu)/a^2; % The non-linear part
dqdt = Ros - J;
```

In this thesis, the diffusion is not used. However, if we want to deal with problems such like energy cascade on the globe, diffusion is needed. The code of diffusion

is rather easy. But the basis we used for calculating the diffusion is the spherical har-

```

for n = 0:n_max
    for m = -n:n
        for ind = 1:n_grid*2
            S(:,ind) = P(:,n+1,m+n_max+1)*exp(1i*m*lambda(ind));
        end
        S_conj = conj(S);
        % Obtain q_mn (Spherical harmonics transform)
        q_mn = sum(sum(q.*S_conj))*dmu*dlambda/(4*pi);
        if m < 0
            D_mn = -q_mn0*Alpha0(n+1,-m+1);
        else
            D_mn = -q_mn0*Alpha0(n+1,m+1);
        end
        % D is the diffusion, K is the diffusion coefficient
        D = D + K*real(S0*D_mn);
    end
end

```

monics, not the spheroidal harmonics.

It is better to calculate the non-linear term by calculating the differentiation of q and ψ in the physical space, rather than using convolution method due to the calculational speed and memory usage. Here we may show how to calculate the non-linear term with convolution method (but not recommended)!

First we transform q and ψ to the spectrum space

$$q = \sum q_{mn} S_{mn} \quad (B.1)$$

$$\psi = \sum \psi_{mn} S_{mn}$$

where $S_{mn} = S_{mn}(\mu, \lambda) = \tilde{S}_{mn}(\mu) e^{im\lambda}$. Plug (B.1) into the non-linear term, we

would get

$$\begin{aligned} \frac{\partial \psi}{\partial \lambda} \frac{\partial q}{\partial \mu} - \frac{\partial \psi}{\partial \mu} \frac{\partial q}{\partial \lambda} &= \sum_{(m_1, n_1)(m_2, n_2)} \psi_{m_1 n_1} q_{m_2 n_2} \left(\frac{\partial S_{m_1 n_1}}{\partial \lambda} \frac{\partial S_{m_2 n_2}}{\partial \mu} \right) \\ &\quad - q_{m_1 n_1} \psi_{m_2 n_2} \left(\frac{\partial S_{m_1 n_1}}{\partial \lambda} \frac{\partial S_{m_2 n_2}}{\partial \mu} \right). \end{aligned} \quad (\text{B.2})$$

The derivations of the harmonics are

$$\begin{aligned} \frac{\partial S_{mn}}{\partial \lambda} &= \frac{\partial (\tilde{S}_{mn} e^{im\lambda})}{\partial \lambda} = im \tilde{S}_{mn} e^{im\lambda} \\ \frac{\partial S_{mn}}{\partial \mu} &= \frac{\partial \tilde{S}_{mn}}{\partial \mu} e^{im\lambda}, \end{aligned} \quad (\text{B.3})$$

substituting (B.3) into (B.2) and using the spectrum invertibility principle (3.4), we

would obtain

$$\begin{aligned} \frac{\partial \psi}{\partial \lambda} \frac{\partial q}{\partial \mu} - \frac{\partial \psi}{\partial \mu} \frac{\partial q}{\partial \lambda} &= -ia^2 \sum_{(m_1, n_1)(m_2, n_2)} q_{m_1 n_1} q_{m_2 n_2} \left(\frac{m_1}{\alpha_{m_1 n_1}} \frac{\partial \tilde{S}_{m_2 n_2}}{\partial \mu} S_{m_1 n_1} \right. \\ &\quad \left. + \frac{m_2}{\alpha_{m_1 n_1}} \frac{\partial \tilde{S}_{m_1 n_1}}{\partial \mu} S_{m_2 n_2} \right) \end{aligned} \quad (\text{B.4})$$

If we aim to calculate the non-linear term of the spectrum $(m, n) = (r, p)$, the formula


is written as

$$\iint \frac{1}{a^2} \left(\frac{\partial \psi}{\partial \lambda} \frac{\partial q}{\partial \mu} - \frac{\partial \psi}{\partial \mu} \frac{\partial q}{\partial \lambda} \right) \tilde{S}_{rp} e^{-ip\lambda} d\mu d\lambda \quad (\text{B.5})$$

Substitute (B.5) with (B.4), and discretize the formula yields

$$\frac{\Delta q_{rp}}{\Delta t} - i \sum_{(m_1, n_1)(m_2, n_2)} \mathbf{D}(n_1, m_1, n_2, m_2; r, p) q_{m_1 n_1} q_{m_2 n_2} = 0 \quad (\text{B.6})$$

where \mathbf{D} is a six-dimensional matrix defined as



$$\begin{aligned}
\mathbf{D}(n_1, m_1, n_2, m_2; r, p) &\equiv \int_{-1}^1 \left(\frac{m_1}{\alpha_{m_1 n_1}} \frac{\partial \tilde{S}_{m_2 n_2}}{\partial \mu} \tilde{S}_{m_1 n_1} \tilde{S}_{rp} \right. \\
&\quad \left. - \frac{m_2}{\alpha_{m_1 n_1}} \frac{\partial \tilde{S}_{m_1 n_1}}{\partial \mu} \tilde{S}_{m_2 n_2} \tilde{S}_{rp} \right) d\mu \int_0^{2\pi} e^{i(m_1+m_2-p)\lambda} \\
&= \int_{-1}^1 \left(\frac{m_1}{\alpha_{m_1 n_1}} \frac{\partial \tilde{S}_{m_2 n_2}}{\partial \mu} \tilde{S}_{m_1 n_1} \tilde{S}_{rp} \right. \\
&\quad \left. - \frac{m_2}{\alpha_{m_1 n_1}} \frac{\partial \tilde{S}_{m_1 n_1}}{\partial \mu} \tilde{S}_{m_2 n_2} \tilde{S}_{rp} \right) d\mu \\
&\quad \cdot \delta_{(m_1+m_2-p)}
\end{aligned} \tag{B.7}$$

Summing up all the spectrums (r, p) would yield the whole dq/dt . The computational complexity would be proportional to the quadrillion of the cutoff wavenumber (since \mathbf{D} is six-dimensional with delta function), so the cost of the computation grows rapidly with the increasing resolution. That is why we should calculate the derivation in the physical space, rather than computing the interaction coefficients in spectrum space.